N-WASP-dependent branched actin polymerization attenuates B-cell receptor signaling by increasing the molecular density of receptor clusters

Anshuman Bhanja[1], Michelle Lazzaro[1,^], Arpita Upadhyaya[2,3,4], and Wenxia Song[1]*

[1]Department of Cell Biology and Molecular Genetics, University of Maryland, College Park, MD 20742, USA

[2]Biophysics Program, University of Maryland, College Park, MD, 20742, USA.

[3]Department of Physics, University of Maryland, College Park, MD, 20742, USA. arpitau@umd.edu.

[4]Institute for Physical Science and Technology, University of Maryland, College Park, MD, 20742, USA.

^ Current address: AstraZeneca, Gaithersburg, MD 20878, United States

* Authors for correspondence: wenxsong@umd.edu and arpitau@umd.edu

Abstract

Antigen-induced B-cell receptor (BCR) signaling is critical for initiating and regulating B-cell activation. The actin cytoskeleton plays essential roles in BCR signaling. Upon encountering cell-surface antigens, actin-driven B-cell spreading amplifies signaling, while B-cell contraction following spreading leads to signal attenuation. However, the mechanism by which actin dynamics switch BCR signaling from amplification to attenuation is unknown. Here, we show that Arp2/3-mediated branched actin polymerization is required for B-cell contraction. Contracting B-cells generate centripetally moving actin foci from lamellipodial F-actin networks in the B-cell plasma membrane region contacting antigen-presenting surfaces. Actin polymerization driven by N-WASP, but not WASP, generates these actin foci. N-WASP-dependent actin foci facilitate non-muscle myosin II recruitment to the contact zone to create actomyosin ring-like structures. Furthermore, B-cell contraction increases BCR molecular density in individual clusters, leading to decreased BCR phosphorylation. Increased BCR molecular density reduced levels of the stimulatory kinase Syk, the inhibitory phosphatase SHIP-1, and their phosphorylated forms in individual BCR clusters. These results suggest that N-WASP-activated Arp2/3 generates centripetally moving foci and contractile actomyosin ring-like structures from lamellipodial networks, enabling contraction. B-cell contraction attenuates BCR signaling by pushing out both stimulatory kinases and inhibitory phosphatases from BCR clusters, providing novel insights into actin-facilitated signal attenuation.

Introduction

B-cell-mediated antibody responses are essential for eliminating invading pathogens. B-cell receptors (BCRs) expressed on the B-cell surface detect the presence of cognate antigens. The binding of antigen to the BCR leads to the activation of signaling cascades (Reth and Wienands 1997; Dal Porto *et al.* 2004; Kwak *et al.* 2019), which induce transcriptional programs that prepare B-cells for proliferation and differentiation (Kurosaki *et al.* 2010; Shlomchik *et al.* 2019; Wang *et al.* 2020). BCR signaling also induces rapid antigen internalization, processing, and presentation for T-cell recognition, which provides the second signal required for B-cell clonal expansion and differentiation to high-affinity antibody-secreting cells and memory B-cells (Song *et al.* 1995; Gitlin *et al.* 2014). BCR signaling is tightly regulated by various external and internal factors to activate antibody responses that are specific and also qualitatively and quantitatively matched to the encountered antigen.

Antigen-induced receptor reorganization activates BCRs at the B-cell surface. Antigen binding leads to BCR clustering at lipid rafts, which enables raft-resident kinases, such as the Src kinases Lyn and Fyn, to phosphorylate immunoreceptor tyrosine-based activation motifs (ITAMs) in the cytoplasmic domains of the BCR signaling subunit CD79a/b heterodimer (Reth 1994; Pierce 2002; Sohn *et al.* 2008). Doubly phosphorylated ITAMs recruit and activate spleen tyrosine kinase (Syk), which in turn activates multiple downstream signaling pathways, including phospholipase Cγ2 (PLCγ2), Bruton's tyrosine kinase (Btk), Ras-GTPase, and phosphatidylinositol-3 kinase (PI3K), initiating signaling cascades (Kurosaki 2000; Dal Porto *et al.* 2004; Tanaka and Baba 2020). Signaling activation also induces the recruitment and activation of inhibitory phosphatases, such as SH2-containing tyrosine phosphatase-1 (SHP-1) and phosphatidylinositol-5 phosphatase-1 (SHIP-1), to BCR signaling complexes (Brauweiler *et al.* 2000; Gross *et al.* 2009; Franks and Cambier 2018). SHIP-1 and SHP-1 negatively regulate

3

64   BCR signaling by inactivating the plasma membrane docking lipids for stimulatory kinases, such

65   as Btk and Akt (Aman *et al.* 1998; Bolland *et al.* 1998) and dephosphorylating BCR and its

66   downstream signaling molecules (Mizuno *et al.* 2000; Adachi *et al.* 2001), respectively. The

67   interplay between the stimulatory kinases and the inhibitory phosphatases controls the balance

68   of antibody responses against pathogens and self. Deficiencies in stimulatory kinases by

69   mutations, such as Btk, cause X-linked agammaglobulinemia (XLA) (Kinnon *et al.* 1993), while

70   deficiencies in the inhibitory phosphatases SHP-1 or SHIP-1 result in autoimmune diseases

71   (Pao *et al.* 2007; Leung *et al.* 2013). However, the mechanisms by which BCR signaling

72   attenuation is initiated and regulated remain elusive.

73

74   B-cells encounter both soluble and membrane-associated antigens *in vivo*. Membrane-

75   associated antigens include antigens on antigen-presenting cells, like follicular dendritic cells in

76   B-cell follicles or germinal centers, and pathogenic cells, like bacteria, parasites, and cancer

77   cells (Batista and Harwood 2009; Depoil *et al.* 2009; Gonzalez *et al.* 2009; Cyster 2010). The

78   binding of multi-valent soluble antigen and membrane-associated antigen with any valency

79   induces dynamic reorganization of surface BCRs into microclusters, triggering BCR signaling.

80   Subsequently, surface BCRs continue moving to the plasma membrane region contacting

81   antigen-presenting surfaces or to one B-cell pole in the case of soluble antigen, which leads to

82   the growth and merger of BCR microclusters and the formation of immunological synapses

83   (Carrasco *et al.* 2004; Harwood and Batista 2010) or supra-molecular activation complexes

84   (Unanue and Karnovsky 1973; Schreiner and Unanue 1977; Tolar *et al.* 2009b; Harwood and

85   Batista 2010).

86

87   Multiple mechanisms have been proposed for signaling initiation by antigen-induced surface

88   BCR reorganization. The binding of surface BCRs to membrane-associated antigen has been

89   shown to induce a conformational change in the BCR extracellular domain, exposing a proximal

4

90   membrane region of membrane IgM that promotes receptor clustering (Tolar *et al.* 2009a; Shen

91   *et al.* 2019). Antigen-binding also changes the conformation of the BCR cytoplasmic domains

92   from a closed to an open form, facilitating the recruitment of signaling molecules (Tolar *et al.*

93   2005). Alternatively, antigen-BCR interaction can increase the molecular spacing of BCRs in

94   clusters, facilitating BCR interaction with signaling molecules (Yang and Reth 2010; Kläsener *et*

95   *al.* 2014). The inhibitory phosphatases SHP-1 and SHIP-1 are also recruited to BCR clusters

96   (Adachi *et al.* 2001; Seeley-Fallen *et al.* 2014). However, the mechanisms underlying

97   phosphatase recruitment and its relationship with BCR signaling activation complexes are

98   unknown.

99

100   The actin cytoskeleton is essential for antigen-induced BCR reorganization on the B-cell surface

101   in response to both soluble and membrane-associated antigen (Harwood and Batista 2011; Liu

102   *et al.* 2013b; Song *et al.* 2013; Hoogeboom and Tolar 2016). Early signaling of the BCR triggers

103   transient actin depolymerization via Rap GTPase and its downstream target cofilin (Freeman *et*

104   *al.* 2011), which disassembles the existing cortical actin network that confines the lateral

105   movement of surface BCRs (Treanor *et al.* 2010). Following this transient depolymerization,

106   BCR signaling activates rapid actin polymerization through the actin nucleation promoting

107   factors Wiskott-Aldrich Syndrome Protein (WASP) and neuronal-WASP (N-WASP), modulating

108   BCR mobility and leading to F-actin accumulation at BCR-antigen interaction sites (Liu *et al.*

109   2013a; Rey-Suarez *et al.* 2020). Actin polymerization and treadmilling in B-cells stimulated by

110   soluble antigen drive surface BCRs to cluster and move to one pole of the B-cell, forming a BCR

111   cap (Schreiner and Unanue 1977; Liu *et al.* 2012a). Upon interacting with membrane-associated

112   antigen, B-cells organize actin into two dynamic structures. One treadmills outwards, driving B-

113   cell membrane spreading and expanding the B-cell membrane region contacting the antigen-

114   presenting surface (contact zone), which enables more BCRs to engage antigen (Bolger-Munro

115   *et al.* 2019). The other creates retrograde flow towards the center of the B-cell contact zone,

5

116   driving the centripetal movement and growth of BCR microclusters (Liu *et al.* 2012b). Together,

117   these processes amplify BCR signaling (Batista *et al.* 2010; Harwood and Batista 2011). The

118   extent of B-cell spreading and the amount of BCR-antigen complexes gathered in the contact

119   zone depend on BCR binding affinity and the density of antigen on the membrane (Fleire *et al.*

120   2006). Subsequent to spreading, B-cells contract, reducing the contact area, which drives BCR

121   microclusters to merge into central clusters to form immunological synapses (Fleire *et al.* 2006;

122   Liu *et al.* 2013a).

123

124   The actin cytoskeleton closely interplays with BCR signaling. We have previously shown that

125   mouse primary B-cells with Btk deficiency (Liu *et al.* 2011) or double knockouts of the actin

126   nucleation promoting factors WASP and N-WASP (Liu *et al.* 2013a) fail to spread on antigen-

127   presenting surfaces and establish stable interactions with membrane-associated antigen,

128   drastically reducing BCR signaling. Btk can activate WASP and N-WASP through Vav, the

129   guanine nucleotide exchange factor of Cdc42 and Rac and phosphatidylinositol-5 kinase that

130   generates phosphatidylinositol-4,5-biphosphate ($PI4,5P_2$) (Sharma *et al.* 2009; Padrick and

131   Rosen 2010). Surprisingly, B-cell-specific knockout of N-WASP (cNKO) but not WASP germline

132   knockout (WKO) enhances B-cell spreading, delays B-cell contraction, and inhibits the

133   centralization of BCR clusters at the contact zone (Liu *et al.* 2013a). Consistent with these

134   findings, Bolger-Munro et al. have shown that knockdown of the actin nucleation factor Arp2/3

135   downstream of WASP and N-WASP disrupts the dynamic actin reorganization induced by

136   membrane-associated antigen required for BCR microcluster growth and merger (Bolger-Munro

137   *et al.* 2019). Using B-cell-specific and germline knockouts, we showed that in addition to N-

138   WASP, the actin motor non-muscle myosin IIA (NMIIA) (Seeley-Fallen *et al.* 2022) and the

139   actin-binding adaptor protein Abp1 (Seeley-Fallen *et al.* 2014) are required for B-cell contraction

140   and BCR central cluster formation. Finally, Wang et al. recently showed that in the presence of

141   the adhesion molecule ICAM on the antigen-presenting surface, B-cells form contractile

6

142   actomyosin arcs, driving centripetal movement of BCR clusters in the B-cell contact zone (Wang

143   *et al.* 2022). Together, these findings indicate a critical role of different actin networks in B-cell

144   contraction and BCR signaling.

145

146   Our previously studies demonstrate that B-cell contraction is critical for BCR signaling

147   attenuation. Delay and inhibition of B-cell contraction through deficiencies of the actin regulators

148   N-WASP, Abp1, or NMIIA, prolongs and/or increases BCR signaling by enhancing the activation

149   of stimulatory kinases and suppressing the activation of inhibitory phosphatases, which elevates

150   the production of autoantibody levels in mice (Liu *et al.* 2013a; Seeley-Fallen *et al.* 2014;

151   Seeley-Fallen *et al.* 2022). N-WASP and NMIIA are not known to interact with kinases and

152   phosphatases directly. The growth, merger, and centralization of antigen-BCR complexes at the

153   B-cell contact zone during the B-cell contraction phase are associated with the reduced BCR

154   signaling capability (Liu *et al.* 2013a). These findings suggest that B-cell contraction is one of

155   the mechanisms for inducing BCR signaling attenuation. However, how the actin cytoskeleton

156   facilitates the transition of the spreading to contraction phase and how B-cell contraction

157   switches BCR signaling from amplification to attenuation is unknown.

158

159   This study explores the mechanisms by which the actin cytoskeleton remodels from spreading

160   lamellipodia to contractile structures and by which B-cell contraction suppresses BCR signaling.

161   Our results show that the contractile actomyosin structures responsible for B-cell contraction

162   originate from branched actin at spreading lamellipodia. N-WASP/Arp2/3- mediated actin

163   polymerization prolongs the lifetime of the lamellipodial actin structures, enables NMIIA

164   recruitment, and drives their movement to the center of the B-cell contact zone. B-cell

165   contraction increases the molecular density within individual BCR-antigen clusters, which

166   promotes the disassociation of both the stimulatory kinase Syk and the inhibitory phosphatases

167   SHIP-1 from BCR clusters, leading to signal attenuation. Our study reveals a new mechanism

168   underlying BCR signal downregulation.

169

170   **Results**

171   **Arp2/3, activated by N-WASP but not WASP, is required for B-cell contraction**

172   Arp2/3-generated branched F-actin is known to drive lamellipodial expansion for B-cell

173   spreading (Bolger-Munro *et al.* 2019). However, whether branched F-actin is involved in the

174   subsequent contraction phase is unknown. To address this, we perturbed the polymerization of

175   branched F-actin using the Arp2/3 inhibitor CK-666 (50 µM) while using its inactive derivative

176   CK-689 as a control. Pre-warmed splenic B-cells from WT C57BL/6 mice were incubated with

177   monobiotinylated Fab' fragment of anti-mouse IgM+G attached to planar lipid bilayers (Fab'-

178   PLB) by biotin-streptavidin interaction and imaged live at 37°C using interference reflection

179   microscopy (IRM). The contact area of B-cells treated with CK-689 rapidly increased upon

180   contacting Fab'-PLB and reached a maximum at ≥0.5 min after the initial contact (*Figure 1A,*

181   *Figure 1-figure supplement 1, and Figure 1-Video 1A*). Following maximal spreading, most B-

182   cells reduced the area of their contact zone, indicating contraction (*Figure 1A, Figure 1-figure*

183   *supplement 1, and Figure 1-Video 1A*). We classified a B-cell as contracting if its contact zone

184   area reduced by ≥5% for at least 10 sec after reaching a maximum value. Based on the average

185   timing for B-cell maximal spreading, we treated B-cells with CK-666 at the beginning of the

186   incubation (Time 0), before B-cell spreading initiation, or at 2 min, when all B-cells had already

187   spread. The effectiveness of CK-666 was detected by reduced Arp2/3 staining in the contact

188   zone (*Figure 1-figure supplement 2*). As expected, CK-666 treatment at 0 but not 2 min reduced

189   the kinetics of B-cell spreading (*Figure 1-figure supplement* 3). Importantly, CK-666 treatment at

190   0 and 2 min both significantly reduced the percentage of B-cells undergoing contraction (*Figure*

191   *1A-C and Figure 1-Video 1A*). The inhibitory effect of CK-666 on B-cell contraction, particularly

8

192   CK-666 treatment after B-cell spreading, suggests that Arp2/3-mediated branched actin

193   polymerization is required for B-cell contraction.

194

195   WASP and N-WASP are actin nucleation-promoting factors upstream of Arp2/3 that are

196   expressed in B-cells (Padrick and Rosen 2010). To determine if either or both were responsible

197   for activating Arp2/3 for B-cell contraction, we utilized the N-WASP inhibitor wiskostatin (Wisko),

198   and splenic B-cells from B-cell-specific N-WASP knockout mice (cNKO) and germline WASP

199   knockout (WKO) mice (Westerberg *et al.* 2012; Liu *et al.* 2013a). Wisko has been shown to

200   inhibit N-WASP activation while enhancing WASP activation in B-cells (*Figure 1-figure*

201   *supplement 4*) (Liu *et al.* 2013a). We found that both Wisko (10 µM) (*Figure 1D and E and*

202   *Figure 1-Video 1B*) and cNKO (*Figure 1F and G and Figure 1-Video 1C*), but not WKO (*Figure*

203   *1H and I and Figure 1-Video 1D*), significantly reduced the percentage of B-cells undergoing

204   contraction, compared to the vehicle, flox, or WT controls. These results suggest that N-WASP-

205   but not WASP-activated Arp2/3 mediates branched actin polymerization for B-cell contraction.

206

207   **Arp2/3, downstream of N-WASP, generates inner F-actin foci, driving B-cell contraction**

208   To understand how Arp2/3 drives B-cells to transition from spreading to contraction, we

209   identified F-actin structures associated with contracting B-cells that were sensitive to CK-666

210   treatment. We visualized F-actin by phalloidin staining and compared F-actin organization in the

211   contact zone of B-cells at the spreading (2 min) and contraction (4 min) phases using TIRF.

212   While B-cells in both spreading and contraction phases exhibited phalloidin staining outlining the

213   contact zone (*Fig. 2A, green arrows*), only B-cells in the contracting phase showed interior

214   phalloidin patches brighter than the phalloidin staining at the periphery of the contact zone

215   (*Figure 2A, purple arrows*). These F-actin patches were organized into a ring-like structure and

216   resided ~1 µm behind the spreading front, surrounding an F-actin-poor center (*Figure 2A, purple*

217   *arrows*). Here, we refer these F-actin patches as inner F-actin foci. We identified inner F-actin

218   foci based on whether their peak fluorescence intensity (FI) was ≥2 fold of the mean

219   fluorescence intensity (MFI) of phalloidin in the no-foci area, had diameters of ≥250 nm, and

220   were located 1 μm away from the edge of the contact zone. We found that such inner F-actin

221   foci were detected in >60% of B-cells in the contracting phase (4 min) but only in <20% of B-

222   cells in the spreading phase (2 min) (*Figure 2B*). CK-666 treatment at 0 min, which inhibited B-

223   cell contraction, significantly reduced the percentage of B-cells showing inner F-actin foci at 4

224   min but not at 2 min (*Figure 2B*). CK-666 treatment did not affect the phalloidin staining outlining

225   the contact zone (*Figure 2A*). Similarly, the percentage of cNKO B-cells showing inner F-actin

226   foci was drastically reduced at 4 min but not at 2 min (*Figure 2C*). These results suggest that the

227   formation of these inner F-actin foci is associated with B-cell contraction.

228

229   We further quantified the number of inner F-actin foci in individual B-cells from mice expressing

230   the LifeAct-GFP transgene (Riedl *et al.* 2010) (*Figure 2D, E, and G*), which allowed us to

231   monitor F-actin reorganization using live-cell imaging (*Figure 2-Video 1*), or using phalloidin

232   staining in flox control and cNKO B-cells (*Figure 2F*). Consistent with the results with phalloidin

233   staining, CK-666 treatment at time 0 significantly reduced the number of inner F-actin foci in the

234   contact zone (*Figure 2D and Figure 1-Video 1A and B*). When we followed the same B-cells

235   before and after CK-666 treatment at 2 min, many of the inner F-actin foci formed before the

236   treatment (1 min 50 sec) disappeared after the treatment (2 min 20 sec), significantly reducing

237   the number of inner F-actin foci (*Figure 2E*). Similar to the CK-666 treatment, cNKO cells

238   significantly reduced the number of inner F-actin foci in the contact zone, compared to flox

239   controls (*Figure 2F*). In contrast, WKO, which does not affect B-cell contraction, did not

240   significantly change the number of inner F-actin foci, compared to WT control B-cells (*Figure 2G*

241   *and Figure 2-Video 1C and D*). Thus, N-WASP- but not WASP-activated Arp2/3 drives the

242   formation and the maintenance of contraction-associated inner F-actin foci.

243

10

244 **Inner F-actin foci are derived from lamellipodial actin networks supporting the spreading**

245 **membrane**

246 We next examined the formation of contraction-associated inner F-actin foci utilizing live-cell

247 TIRF imaging of B-cells from mice expressing LifeAct-GFP. We generated kymographs along

248 eight lines from the center of each contact zone using time-lapse images of LifeAct-GFP (*Figure*

249 *3A and B and Figure 3-figure supplement 1*). Analysis of these kymographs showed that most

250 F-actin foci were first detected closely behind lamellipodial F-actin networks. Following maximal

251 spreading, these F-actin foci moved centripetally while increasing in intensity, becoming inner F-

252 actin foci, in cells transitioning from spreading to contraction (*Figure 3B, top panel, and Figure*

253 *3-figure supplement 1*). However, such centripetally moving F-actin foci were not detected in B-

254 cells that did not undergo contraction (*Figure 3B, bottom panel*). We quantified the percentage

255 of the eight kymographs from each cell that exhibited lamellipodia-derived inner F-actin foci and

256 found, on average, that six out of eight kymographs from contracting cells showed lamellipodia-

257 derived inner F-actin foci, compared to only one or two kymographs from non-contracting cells

258 (*Figure 3C*). To examine the temporal relationship between the generation of lamellipodia-

259 derived inner F-actin foci and contraction, we plotted the percentage of kymographs with

260 lamellipodia-derived inner F-actin foci over time with the spreading to contracting transition time

261 set as 0 (*Figure 3D*). We found that the percentage of kymographs showing lamellipodia-derived

262 inner F-actin foci peaked at almost the same time when the spreading transitioned to

263 contraction (*Figure 3D*), suggesting a close temporal relationship between the two events.

264 Furthermore, the N-WASP inhibitor Wisko, but not WKO, significantly inhibited the formation of

265 lamellipodia-derived inner F-actin foci (*Figure 3E*). Thus, inner F-actin foci originate from

266 branched actin driven lamellipodia and form simultaneously with the transition of B-cell

267 spreading to contraction.

268

11

N-WASP-activated Arp2/3 generates inner F-actin foci by sustaining the lifetime and the

centripetal movement of lamellipodial F-actin

We examined the mechanism by which N-WASP and Arp2/3 generate inner F-actin foci by

measuring their relative lifetime and mobility using kymographs generated from TIRF time-lapse

images of B-cells expressing LifeAct-GFP. Inner F-actin foci were identified as described above,

and their tracks were manually determined (*Figure 4A, black dashed lines*). The time window in

which an inner F-actin patch could be detected in a kymograph was measured as the relative

lifetime, as actin foci could move away from the kymograph line or the TIRF evanescent field

(*Figure 4A, right panels*). The distance each F-actin focus moved during its lifetime was used to

calculate its speed (*Figure 4A, right panels*). Compared to CK-689-treated B-cells, CK-666

treatment at time 0 significantly reduced the relative lifetime and the centripetal speed of inner

F-actin foci (*Figure 4B-D*). After B-cells were treated with CK-666 at 2 min (the average time for

B-cells to reach the maximal spreading), the relative lifetime and the centripetal speed of inner

F-actin foci were significantly lower than before the treatment in the same cell (*Figure 4E-G,*

line-linked dots). Similarly, the N-WASP inhibitor Wisko significantly reduced the relative lifetime

and the centripetal speed of inner F-actin foci (*Figure 4H-J*); however, WKO had no significant

effect (*Figure 4K-M*). These results show that N-WASP and Arp2/3 mediated branched actin

polymerization prolongs the lifetime of lamellipodia-derived F-actin foci and drives them to move

inward in the B-cell contact zone.

Inner F-actin foci, generated by N-WASP-activated Arp2/3, facilitate NMII recruitment and

reorganization into ring-like structures

As non-muscle myosin II (NMII) is required for B-cell contraction (Seeley-Fallen *et al.* 2022), we

examined the relationship between the formation of inner F-actin foci and the recruitment and

reorganization of NMII in the contact zone using TIRF imaging of B-cells from mice expressing a

GFP-NMIIA transgene. Upon interacting with Fab'-PLB, the GFP-NMIIA MFI in the contact zone

12

295   of untreated WT B-cells increased rapidly in the first minute and slowly afterward (*Figure 5A and*

296   *B and Figure 5-Video 1*). Wiskostatin treatment significantly reduced the GFP-NMIIA MFI in the

297   contact zone (*Figure 5B*) and its initial rate of increase (as determined by the slope of the GFP-

298   NMIIA MFI increase at 0~30 sec time window) (*Figure 5C*). Kymographs generated from time-

299   lapse TIRF images of B-cells from mice expressing GFP-NMIIA and LifeAct-RFP showed that

300   recruited NMIIA accumulated between lamellipodia and inner F-actin foci when the foci moved

301   centripetally away from lamellipodia (*Figure 5D, white arrow, and Figure 5-Video 1*). Recruited

302   NMIIA reorganized with inner F-actin foci to form a ring-like structure in the contact zone (*Figure*

303   *5A, D, and E, and Figure 5-Video 1*). The percentage of B-cells with NMIIA ring-like structures,

304   visualized by immunostaining, increased over time as more B-cells underwent contraction

305   (*Figure 5E and F*). Compared to flox controls, the percentage of cNKO B-cells with NMIIA ring-

306   like structures was significantly decreased (*Figure 5E and F*). Wiskostatin treatment also

307   reduced NMIIA recruitment and ring-like structure formation (*Figure 5-Video 1*). Surprisingly, the

308   percentage of WKO B-cells with NMIIA ring-like structure was higher than that of flox control B-

309   cells (*Figure 5E and F*). Thus, N-WASP and Arp2/3 mediated branched actin polymerization

310   promotes the recruitment and the reorganization of NMII ring-like structures by generating inner

311   F-actin foci in the contact zone.

312

313   **B-cell contraction increases the BCR molecular density in individual clusters**

314   To understand how B-cell contraction promotes BCR signaling attenuation, we examined the

315   impact of B-cell contraction on the properties of BCR clusters. We first measured the MFI of

316   AF546-Fab' attached to PLB gathered by B-cells into the contact zone as an indication of the

317   overall BCR molecular density. The clustering of AF546-Fab' on PLB by B-cell binding reflects

318   surface BCR clustering, as B-cell binding to transferrin (Tf)-tethered PLB does not cause

319   surface BCRs to cluster and be phosphorylated (*Figure 6-figure supplement 1*) (Liu *et al.* 2011;

320   Liu *et al.* 2013a). The MFI of AF546-Fab' in the B-cell contact zone increased over time.

321   Treatment with CK-666, Wisko, or cNKO all reduced the AF546-Fab' MFI, particularly during the

322   time window of B-cell contraction in controls (*Figure 6A-G, purple rectangles, and Figure 6-*

323   *Video 1*). Notably, the rates of increase in AF546-Fab' MFI, calculated from the slopes of

324   AF546-Fab' MFI versus time plots in individual cells, were significantly higher during B-cell

325   contraction than before B-cell contraction in control cells and conditions (*Figure 6D-K*).

326   Significantly, inhibiting B-cell contraction by CK-666 treatment at 0 (*Figure 6A, D, and H, and*

327   *Figure 6-Video 1A and D*) or 2 min (*Figure 6A, E, and I*), Wisko (*Figure 6B, F, and J, and Figure*

328   *6-Video 1B and E*), and cNKO (*Figure 6C, G, and K, and Figure 6-Video 1C and F*) abolished

329   the increases in AF546-Fab' accumulation rates. We further examined the peak FI of AF546-

330   Fab' in individual microclusters as a measure of the BCR molecular density in individual

331   clusters. AF546-Fab' clusters were identified based on their diameters $\geq$250 nm, peak FI $\geq$1.1

332   fold outside the B-cell contact zone, and trackable for ≥20 sec (*Figure 6L and Figure 6-figure*

333   *supplement 2*). AF546-Fab' microclusters could not be identified during the early stage of B-cell

334   spreading. Time-lapse imaging by TIRF enabled us to measure the rate of increase in AF546-

335   Fab' peak FI in individual clusters (*Figure 6M and Figure 6-figure supplement 2*). Consistent

336   with our observation of AF546-Fab' MFI increase in the contact zone, the peak FI of individual

337   clusters increased at a faster rate during contraction than after contraction (when the contact

338   area no longer decreased) (*Figure 6N*). Furthermore, CK-666 (*Figure 6O*), Wisko (*Figure 6P*),

339   and cNKO (*Figure 6Q*) all significantly reduced the rate of increase in AF546-Fab' peak FI in

340   individual clusters. These results show that B-cell contraction significantly increases the

341   molecular density of BCRs in BCR clusters.

342

343   **Increased BCR molecular density by B-cell contraction reduces BCR phosphorylation**

344   **levels in individual microclusters**

345   To examine how BCR molecular density influenced BCR signaling capability, we

346   immunostained B-cells interacting with AF546-Fab'-PLB for 1, 3, 5, and 7 min, for

14

347   phosphorylated CD79a (pCD79a, Y182) and performed IRM and TIRF imaging (*Figure 7A and*

348   *H*). We analyzed equal numbers of AF546-Fab' clusters selected randomly, in the contact zone

349   of B-cells interacting with Fab'-PLB for 1, 3, 5, and 7 min, using a gradient threshold of their

350   AF546-Fab' MFI, 1.1 to 4.1 fold of the background, and with diameter ≥250 nm (*Figure 6-figure*

351   *supplement 2*). We determined the MFI of pCD79a and AF546-Fab' in individual clusters and

352   plotted the MFI ratio of pCD79a relative to AF546-Fab' (reflecting the relative level of BCR

353   phosphorylation) versus the AF546-Fab' peak FI (reflecting BCR molecular density) in individual

354   clusters (*Figure 7B and C*). The dot plots show that when the AF546-Fab' peak FI of individual

355   clusters was relatively low, the MFI ratios of pCD79a to AF546-Fab' increased with the AF546-

356   Fab' peak FI in individual clusters of flox control B-cells (*Figure 7B*). When the AF546-Fab' peak

357   FI reached a certain level, the MFI ratios of pCD79a to AF546-Fab' decreased as the AF546-

358   Fab' peak FI in individual clusters further increased (*Figure 7A and B*). Inhibition of B-cell

359   contraction by cNKO reduced the AF546-Fab' peak FI in individual clusters, maintaining it within

360   a relatively low range, where the MFI ratios of pCD79a to AF546-Fab' increased with the

361   AF546-Fab' peak FI (*Figure 7C and D*). Additionally, the average pCD79a to Fab' MFI ratios

362   were much higher in cNKO B-cells than flox control B-cells, when comparing AF546-Fab'

363   clusters with the same range of peak FI (*Figure 7B-D*). During the contraction stage (5 and 7

364   min), flox control B-cells exhibited increased AF546-Fab' MFI (*Figure 7E*) but decreased

365   pCD79a MFI (*Figure 7F*) and the MFI ratios of pCD79a relative to AF54-Fab' (*Figure 7G*) in

366   individual clusters, compared to the spreading stage (1 and 3 min). In contrast, non-contracting

367   cNKO B-cells only slightly increased AF546-Fab' MFI (*Figure 7E*) but significantly increased

368   pCD79a MFI (*Figure 7F*) and the pCD79a to AF546-Fab' MFI ratios (*Figure 7G*) in individual

369   clusters at the contraction stage compared to the spreading stage. Consequently, individual

370   clusters in non-contracting cNKO B-cells had significantly lower AF546-Fab' MFI but

371   significantly higher pCD79a MFI and pCD79a to AF546-Fab' FIRs than contracting flox control

372   B-cells at 5 and 7 min but not at 1 and 3 min (*Figure 7E-G*). Similarly, inhibiting B-cell

15

373   contraction by treatment with the Arp2/3 inhibitor CK-666 at 2 min post-stimulation reduced

374   AF546-Fab' MFI (*Figure 7I*) but increased pCD79a MFI (*Figure 7J*) and the MFI ratios of

375   pCD79a relative to AF546-Fab' (*Figure 7K*) in individual clusters. These data suggest that

376   increases in BCR molecular density in BCR clusters during B-cell contraction inhibit BCR

377   phosphorylation.

378

379   **Increased BCR molecular density by B-cell contraction promotes the disassociation of**

380   **the stimulatory kinase Syk from BCR microclusters**

381   Increased BCR molecular density may promote signaling attenuation by inducing the

382   disassociation and/or dephosphorylation of stimulatory kinases from and at BCR clusters. To

383   test this hypothesis, we analyzed the relative amounts of Syk, a major stimulatory kinase in the

384   BCR signaling pathway, and its phosphorylated form pSyk (Y519/520) in individual BCR

385   clusters in relation to the molecular density of BCRs. Splenic B-cells were incubated with Fab'-

386   PLB for 3 and 7 min (when most cells were at the spreading and contraction phase,

387   respectively), fixed, permeabilized, stained for Syk or pSyk, and imaged using TIRF. We

388   measured MFI ratios of Syk relative to AF546-Fab' in individual BCR clusters to reflect the

389   relative amount of Syk associated with individual BCR clusters and analyzed their relationship

390   with AF546-Fab' peak FI (reflecting the molecular density within BCR clusters). AF546-Fab'

391   clusters were detected and analyzed as described above. In flox control B-cells, the highest

392   fractions of BCR clusters had an AF546-Fab' peak FI at the150~200 range (*Figure 8A, brown*

393   *line and symbol*s). The average MFI ratios of Syk to Fab' in individual clusters increased at a

394   low peak FI range (<140) and did not significantly decrease until Fab' peak FI reached a

395   relatively high range (>280) (*Figure 8A, black line and symbol*). B-cells from cNKO mice

396   exhibited a reduction in the Fab' peak FI of clusters (*Figure 8B and C, brown line and symbol*)

397   but an increase in the average Syk to Fab' MFI ratios in clusters in a wide range of Fab' peak FI,

398   when compared to flox control B-cells (*Figure 8B and C, black lines and symbols*). However, the

399   average Syk to Fab' MFI ratios of cNKO B-cells decreased in clusters with Fab' peak FI $\geq$220

400   and reduced to levels similar to those in flox control B-cells in clusters with Fab' peak FI $\geq$240

401   (*Figure 8B and C, black lines and symbols*). These data suggest that increases in the molecular

402   density of BCR clusters, reflected by Fab' peak FI, induce disassociation of Syk from BCR

403   clusters in both flox control and cNKO B-cells. Our results also show that BCR clusters in cNKO

404   B-cells have significantly higher levels of Syk association than in flox control B-cells, even

405   though they have similar Fab' peak intensities.

406

407   We next analyzed the relationship of the pSyk level in individual clusters with BCR molecular

408   density using the method described above. We found that the MFI ratios of pSyk relative to

409   AF546-Fab' gradually decreased with increases in Fab' peak FI in both flox control and cNKO

410   B-cells (*Figure 8D and E, black lines and symbols*), even though we did not observe an increase

411   in pSyk to Fab' MFI ratio at the low Fab' peak FI range. Similar to the Syk to Fab' MFI ratio, the

412   average pSyk to Fab' MFI ratios of individual clusters in cNKO B-cells were much higher than

413   those in flox control B-cells, except for those at the high Fab' peak FI range (*Figure 8D-F*). To

414   confirm this result, we analyzed equal numbers of pSyk clusters in the same cells, based on the

415   criteria of $\geq$1.3 fold increase in the peak FI compared to the background outside the contact

416   zone with a diameter of $\geq$250 nm. Similar to clusters identified by AF546-Fab', the average MFI

417   ratios of pSyk to Fab' in these pSyk clusters decreased with increase in their Fab' peak FI in

418   both flox control and cNKO B-cells (*Figure 8G-I, black lines and symbols*). Again, the average

419   pSyk to Fab' MFI ratios of pSyk clusters were much higher in cNKO than flox control B-cells, but

420   were reduced to similar levels in clusters with relatively high Fab' peak FI (*Figure 8I, black line

421   and symbols*). Similar reductions of total Syk and pSyk with increasing molecular density of

422   BCR clusters suggest that the disassociation of Syk from BCR clusters, caused by cell

423   contraction-induced increases in molecular density, contributes to BCR signaling attenuation.

17

424

Increased BCR molecular density by B-cell contraction promotes disassociation of the

inhibitory phosphatase SHIP-1 from BCR microclusters

The inhibitory phosphatase SHIP-1 is essential for B-cell signaling attenuation (Brauweiler *et al.*

2000; Liu *et al.* 2011), suggesting that increases in the molecular density of BCR clusters by B-

cell contraction may promote SHIP-1 recruitment. We used the methods described above to

address this hypothesis, staining cells for total SHIP-1 and phosphorylated SHIP-1 (pSHIP-1

Y1020). We found that the average SHIP-1 to Fab' MFI ratios in both flox control and cNKO B-

cells decreased with Fab' peak FI at similar rates (*Figure 9A-C, black lines and symbols*), even

though inhibition of contraction by cNKO reduced the Fab' peak FI of BCR clusters (*Figure 9A-*

C, brown lines and symbols). Notably, the reduction in the SHIP-1 to Fab' MFI ratios with

increasing Fab' peak FI occurred at the lowest detectable Fab' peak PI (*Figure 9A-C, brown*

lines and symbols), when the Syk to Fab' MFI ratios increased and were sustained (*Figure 8A-*

C). Furthermore, this reciprocal relationship between the SHIP-1 to Fab' MFI ratio and Fab'

peak FI continued over the entire Fab' peak FI range. It also remained the same in both flox

control and cNKO B-cells (*Figure 9A-C*). These results suggest that SHIP-1 disassociates from

BCR clusters as their molecular density increases, and that the SHIP-1 disassociation is more

sensitive to the molecular density of BCR clusters than Syk disassociation.

442

Similar to the relationship of total SHIP-1 with BCR molecular density, the average MFI ratios of

pSHIP-1 relative to AF546-Fab' in individual Fab' clusters decreased with increases in Fab'

peak FI at similar rates in flox control and cNKO B-cells (*Figure 9D-F, black lines and symbols*),

even though inhibition of contraction by cNKO reduced Fab' peak FI of BCR clusters (*Figure*

9D-F, brown lines and symbols). The average pSHIP-1 to Fab' MFI ratios in individual pSHIP-1

clusters, detected and analyzed in the same way as pSyk clusters, showed the same decrease

with increases in their Fab' peak FI in both flox control and cNKO B-cells (*Figure 9G-I, black*

450　　*lines and symbols*). Notably, the average pSHIP-1 to Fab' MFI ratios in individual Fab' or

451　　pSHIP-1 clusters in flox control and cNKO B-cells were at similar levels at the same Fab' peak

452　　FI ranges (*Figure 9F and I, black lines and symbols*). These results indicate that contraction-

453　　induced molecular density increases within individual BCR clusters do not induce preferential

454　　recruitment of SHIP-1; instead, it promotes the disassociation of SHIP-1 from BCR clusters.

455

456　　**Discussion**

457　　When binding membrane-associated antigen, B-cells undergo actin-mediated spreading

458　　followed by a contraction, which amplifies BCR signaling and promotes immunological synapse

459　　formation (Fleire *et al.* 2006; Harwood and Batista 2011). We previously showed that B-cell

460　　contraction after spreading on antigen-presenting surfaces promotes BCR signaling attenuation

461　　(Liu *et al.* 2013a; Seeley-Fallen *et al.* 2022). However, how the actin cytoskeleton reorganizes

462　　as B-cells transition from spreading to contraction and how B-cell contraction downregulates

463　　BCR signaling have been elusive. Here we demonstrate that inner F-actin foci formed at the

464　　contact zone distal to the lamellipodial F-actin network promote B-cells to switch from spreading

465　　to contraction. These inner foci are derived from the lamellipodial F-actin network that mediates

466　　spreading, are generated by N-WASP- but not WASP-activated Arp2/3-mediated branched actin

467　　polymerization, and facilitate NMII recruitment, enabling B-cell contraction. B-cell contraction

468　　increases BCR molecular density in existing clusters, which promotes the disassociation of both

469　　the stimulatory kinase Syk and the inhibitory phosphatase SHIP-1, leading to signaling

470　　attenuation.

471

472　　One significant finding of this study is that Arp2/3-mediated polymerization of branched actin is

473　　required for B-cell contraction. Arp2/3-mediated branched actin polymerization is known to drive

474　　B-cell spreading and to create actin centripetal flow at the contact zone between B-cells and

475　　antigen-presenting surface (Bolger-Munro *et al.* 2019). The actin structure that supports B- and

476   T-cell spreading to form the immunological synapse with antigen-presenting cells is similar to

477   lamellipodial F-actin networks found in adherent cells (Bunnell *et al.* 2001; Koestler *et al.* 2008;

478   Bolger-Munro *et al.* 2019). Lamellipodial F-actin networks consist primarily of branched actin

479   filaments polymerizing against the plasma membrane interspersed with bundled actin filaments

480   (Krause and Gautreau 2014; Skau and Waterman 2015). Contractile actin structures, such as

481   stress fibers, are typically generated from bundled actin filaments, as observed in adherent and

482   migrating cells (Levayer and Lecuit 2012; Tojkander *et al.* 2015; Hammer *et al.* 2019). Here, we

483   show that inner F-actin foci, generated by Arp2/3-mediated actin polymerization, transition B-

484   cells from spreading to contraction. Furthermore, these inner F-actin foci are directly derived

485   from lamellipodial F-actin networks. Based on the observed dynamics, we infer that instead of

486   polymerizing against the plasma membrane, Arp2/3 appears to nucleate actin polymerization in

487   the opposite direction, sustaining actin foci and their movement away from the lamellipodia.

488   However, this study does not exclude the involvement of bundled actin filaments. Based on the

489   requirement of formin-activated bundled actin filaments for lamellipodial F-actin networks and B-

490   cell spreading (Wang *et al.* 2022), we can speculate that bundled actin filaments may play a role

491   in the formation and movement of these inner F-actin foci, as well as in NMII recruitment.

492

493   Our work provides new insights into distinct functions of the actin nucleation-promoting factors

494   WASP and N-WASP in controlling cell morphology and signaling. Immune cells, including B-

495   cells, express both hematopoietic-specific WASP and the ubiquitous homolog of WASP, N-

496   WASP. These two share high sequence homology, activation mechanism, and Arp2/3 activation

497   function (Padrick and Rosen 2010). We previously identified distinct functions of these two

498   factors that are unique to B-cells. While both are required for B-cell spreading, N-WASP plays a

499   unique role in B-cell contraction. WASP and N-WASP double knockout B-cells fail to spread on

500   antigen-presenting surfaces, but B-cell-specific N-WASP knockout enhances B-cell spreading

501   and delays B-cell contraction (Liu *et al.* 2013a). Furthermore, these two factors reach peak

20

502   activation at different times (phosphorylated WASP peaks during B-cell spreading, while

503   phosphorylated N-WASP peaks during contraction) and are detected at distinct locations (the

504   majority of WASP is at the periphery, and N-WASP is scattered across the B-cell contact zone)

505   (Liu *et al.* 2013a). Here, we reveal the exact role of N-WASP in B-cell contraction – to generate

506   inner F-actin foci from lamellipodial F-actin networks by activating Arp2/3-mediated actin

507   polymerization. N-WASP- but not WASP-activated actin polymerization prolongs the relative

508   lifetime of actin foci and mediates their inward motion toward the center of the contact zone. The

509   delayed activation time and the location in the interior of the contact zone likely give N-WASP a

510   unique opportunity to generate inner F-actin foci. As WASP and N-WASP suppress each other

511   for activation in B-cells (Liu *et al.* 2013a), the timing and the location of their activation may

512   depend on the relative levels of their expression and their abilities to compete for upstream and

513   downstream molecules. As cNKO only delays and reduces but does not block B-cell contraction

514   and inner F-actin foci formation, other actin factors may be involved, such as the WASP-family

515   verprolin-homologous protein (WAVE) (Rotty *et al.* 2013).

516

517   Our recently published data show that NMII is required for B-cell contraction. Activated NMII is

518   recruited to the B-cell contact zone in a SHIP-1-dependent manner and forms a peripheral ring

519   surrounding the contact zone during B-cell contraction (Seeley-Fallen *et al.* 2022). Here, we

520   further show that in addition to SHIP-1, N-WASP but not WASP is also involved in NMII

521   recruitment and NMII ring-like structure formation, probably by generating inner F-actin foci.

522   Collectively, these findings suggest that SHIP-1 coordinates with N-WASP to recruit NMII. Our

523   previous finding that SHIP-1 promotes B-cell contraction by facilitating N-WASP activation (Liu

524   *et al.* 2011; Liu *et al.* 2013a) supports this notion. However, it is surprising that the recruitment of

525   NMII activated by BCR signaling to the contact zone is associated with inhibitory signaling

526   molecules. BCR downstream signaling, including Ca^{2+} fluxes and Rho-family GTPase activation,

527   likely activates NMII motor activity (Vicente-Manzanares *et al.* 2009). The activation switches

21

528   NMII from the incompetent folded conformation to the competent extended conformation,

529   enabling NMII molecules to bind to F-actin and assemble into contractible bipolar filaments and

530   stacks (Matsumura 2005). A denser F-actin organization has been shown to increase NMII

531   filament stacking (Fenix and Burnette 2018). Here, we showed that the inner F-actin foci

532   generated by N-WASP-activated Arp2/3 are more stable and denser and thus likely promote

533   NMII binding and stacking more efficiently than F-actin generated by WASP-activated Arp2/3.

534   Indeed, our kymograph analysis revealed similar time windows and spatial locations for NMII

535   accumulation and for generating inner F-actin foci from lamellipodial F-actin, supporting our

536   hypothesis.

537

538   Wang et al. (Wang *et al.* 2022) recently showed that B-cells generate actomyosin arcs when

539   interacting with membrane-associated antigen in the presence of adhesion molecules, as when

540   interacting with professional antigen-presenting cells. In contrast to T-cells, B-cells can also

541   respond to membrane-associated antigen without the help of adhesion molecules, when

542   engaging antigen on pathogenic cells, like bacteria, parasites, and cancer cells. While the

543   relationship between actomyosin arcs and inner F-actin foci remains to be explored, the role of

544   inner F-actin foci in the formation of NMII ring-like structures revealed in our study suggests that

545   the inner F-actin foci in the absence of adhesion molecules may be the facilitator or precursors

546   of the actomyosin arcs. These structures can potentially be enhanced and matured by

547   interactions between B-cells and antigen-presenting membranes mediated by adhesion

548   molecules.

549

550   Our findings suggest an increase in the molecular density within BCR clusters or B-cell

551   synapses as one of the mechanisms by which B-cell contraction promotes BCR signaling

552   attenuation. During contraction, the molecular density of individual BCR clusters, measured by

553   their MFI and peak FI of BCR clustered Fab', increased faster than during the spreading and

22

554   post-contraction phases. Surprisingly, increases in molecular density induced disassociation of

555   both the stimulatory kinase Syk and the inhibitory phosphatase SHIP-1, contradicting the

556   existing dogma of sequential association of stimulatory and inhibitory signaling molecules with

557   the BCR (Franks and Cambier 2018). Interestingly, the disassociation of SHIP-1 is much more

558   sensitive to BCR molecular density than Syk disassociation. Syk does not disassociate until the

559   molecular density of BCR clusters reaches the top 10% range, while SHIP-1 disassociates from

560   BCR clusters with increases over the entire detectable range of molecular densities. When B-

561   cell contraction is inhibited, the molecular density of BCR clusters is reduced to a range with

562   limited Syk disassociation and normal SHIP-1 disassociation, resulting in high Syk to SHIP-1

563   molecular ratios in BCR clusters than contracting B-cells, increasing BCR signaling levels. The

564   resolution of our widefield TIRF imaging limits our ability to examine nascent BCR clusters that

565   actively recruit signaling molecules. However, the consistency of the data from AF546-Fab' and

566   pSyk or pSHIP-1 clusters confirms our results. How the molecular density within BCR clusters

567   promotes disassociation of signaling molecules is unknown. We speculate that molecular

568   crowding may displace signaling molecules out of BCR clusters. Supporting this possibility,

569   disassociation of the 145 kDa SHIP-1 is likely to be more sensitive to changes in the molecular

570   density of BCR clusters, compared to disassociation of the 72 kDa Syk. However, these

571   hypotheses need to be further examined.

572

573   An interesting finding of this study is that the pCD79a and pSyk levels were higher in individual

574   BCR clusters of cNKO B-cells than those of flox control B-cells, even when BCR clusters had

575   similar molecular densities. These data suggest additional mechanisms for B-cell contraction to

576   promote BCR signaling attenuation. In addition to increasing molecular density within BCR

577   clusters, the contractile forces generated by actomyosin rings on the B-cell membrane and BCR

578   clusters may cause changes to the conformations of both BCRs and associated signaling

579   molecules and their lateral interactions in the membrane. These changes may favor the

23

580   disassociation rather than the association of signaling molecules with BCR clusters. Recently

581   solved molecular assembly structures of both human and mouse BCRs (Dong *et al.* 2022; Su *et*

582   *al.* 2022) support conformational and lateral molecular interaction changes as possible

583   mechanisms for BCR signaling regulation. Actomyosin-mediated contractile forces were also

584   shown to be required for BCR-mediated endocytosis of antigen (Natkanski *et al.* 2013;

585   Hoogeboom *et al.* 2018; Maeda *et al.* 2021), which removes the BCR from the cell surface,

586   downregulating the BCR surface signaling. Whether the inner F-actin foci identified here play

587   any role in BCR endocytosis remains an interesting question. Our early finding that N-WASP is

588   required for BCR endocytosis (Liu *et al.* 2013a) supports this notion. Similar to the differential

589   impact of the molecular density on the disassociation of Syk and SHIP-1 from BCR clusters, B-

590   cell contraction may differentially affect the interaction of surface BCRs with cytoplasmic and

591   membrane-anchored signaling molecules, such as the lipidated and lipid raft-resident Src kinase

592   Lyn that is responsible for phosphorylating both the immunoreceptor tyrosine-based activation

593   motif (ITAM) of CD79a and the immunoreceptor tyrosine-based inhibitory motif (ITIM) that SHIP-

594   1 binds to (Franks and Cambier 2018).

595

596   The results presented here have revealed novel insights into the mechanisms underlying actin-

597   facilitated signaling attenuation of the BCR. Taking our previous and current data together, we

598   propose a new working model for such actin-mediated signaling downregulation. Upon maximal

599   spreading, N-WASP distal to lamellipodial networks activates Arp2/3-mediated branched actin

600   polymerization, which sustains actin foci originating from lamellipodia and their movement away

601   from the lamellipodia towards the center of the B-cell contact zone, generating inner F-actin foci.

602   NMII is then preferentially recruited to these relatively stable inner foci, forming ring-like

603   actomyosin structures, which enable B-cell contraction. B-cell contraction pushes the BCR

604   microclusters formed during B-cell spreading to the center of the contact zone, increasing their

605   molecular density. Increased molecular density promotes disassociation of signaling molecules

24

606   from BCR clusters, probably due to crowding and conformational changes, leading to signal

607   downregulation. Inhibitory signaling molecules likely activate the actin reorganization that drives

608   B-cell contraction, as both the activation of N-WASP and the recruitment of NMII to the B-cell

609   contact zone depend on SHIP-1 (Liu *et al.* 2013a; Seeley-Fallen *et al.* 2022). Thus, actin

610   reorganization downstream of inhibitory phosphatases reinforces signaling attenuation by

611   driving B-cell contraction.

612

613   **Materials and Methods**

614   Key Reagents Table

Reagent type	Designation	Source	Identifiers	Additional Information
B-cells from C57BL/6 mice	WT	Jackson Laboratories	000664	
B-cells from WASP$^{-/-}$ mice	WKO	Jackson Laboratories	019458	
B-cells from CD19$^{Cre/+}$N-WASP$^{flox/flox}$ mice	cNKO	Lisa Westerberg laboratory		
B-cells from N-WASP$^{flox/flox}$ mice	Flox control	Lisa Westerberg laboratory		
B-cells from LifeAct-GFP mice	LifeAct-GFP	Roberto Weigert laboratory		
B-cells from LifeAct-RFP mice	LifeAct-RFP	Klaus Ley laboratory		
B-cells from GFP-NMIIA mice	GFP-NMIIA	Robert Adelstein laboratory		
Reagent	1,2-dioleoyl-sn-glycero-3-phosphocholine	Avanti Polar Lipids	850375 P	5 mM
Reagent	1,2-dioleoyl-sn-glycero-3-phosphoethanolamine-cap-biotin	Avanti Polar Lipids	870273 C	50 µM
Reagent	Streptavidin	Jackson Immuno Research	016-000-084	1 µg/ml
Antibody	F(ab')$_2$ fragment of goat IgG anti-mouse Ig(G+M) (polyclonal)	Jackson Immuno Research	115-006-068	-
Antibody	Cy3-Fab fragment of goat anti-mouse IgG+M (polyclonal)	Jackson Immuno Research	115-167-020	2.5 µg per 1 x 10^6 cells

25

Chemical	2-Mercaptoethylamine HCL	Thermo Fisher Scientific	20408	50 mM
Reagent	EZ-Link™ Maleimide-PEG$_2$-biotin	Thermo Fisher Scientific	A39261	20 mM per mM of protein
Commercial Kit	Alexa Fluor 546 antibody labeling kit	Thermo Fisher Scientific	A20183	-
Ligand	Biotinylated holo-transferrin	Jackson Immuno Research	015-060-050	-
Antibody	Rat IgG$_{2b}$ anti-mouse CD90.2 (Thy1.2) (monoclonal)	Biolegend	105351	1 µl per 2×10^6 cells
Inhibitor	CK-689	Millipore Sigma	182517-25MG	50 µM
Inhibitor	CK-666	Millipore Sigma	SML0006-5MG	50 µM
Inhibitor	Wiskostatin	Millipore Sigma	W2270-5MG	10 µM
Antibody	Rabbit IgG anti-mouse Arp2 antibody (polyclonal)	Abcam	ab47654	1:100
Antibody	Rabbit IgG anti-mouse pWASP antibody (polyclonal)	Thermo Fisher Scientific	PA5-105572	1:100
Antibody	Rabbit IgG anti-mouse pN-WASP antibody (polyclonal)	Thermo Fisher Scientific	PA5-105307	1:100
Antibody	AF488-goat IgG anti-rabbit IgG antibody (polyclonal)	Thermo Fisher Scientific	A-11034	1:200
Antibody	AF546-goat IgG anti-rabbit IgG antibody (polyclonal)	Thermo Fisher Scientific	A-11035	1:200
Reagent	Acti-stain-488 Phalloidin	Cytoskeleton	PHDG1-A	200 nM
Reagent	Acti-stain-555 Phalloidin	Cytoskeleton	PHDH1-A	200 nM
Antibody	Rabbit IgG anti-mouse NMIIA antibody (polyclonal)	Abcam	ab75590	1:100
Antibody	Rabbit IgG anti-mouse pCD79a (Y182) (monoclonal)	Cell Signaling Technology	14732S	1:100
Antibody	Rabbit IgG anti-mouse pSyk (Y519/520) (monoclonal)	Cell Signaling Technology	2710S	1:100
Antibody	Rabbit IgG anti-mouse pSHIP-1 (Y1020) (polyclonal)	Cell Signaling Technology	3941S	1:100
Antibody	Rabbit IgG anti-mouse Syk (polyclonal)	Thermo Fisher Scientific	PA5-17812	1:100
Antibody	Rabbit IgG anti-mouse SHIP-1 (polyclonal)	Thermo Fisher Scientific	PA5-115894	1:100

615

Mice and B-cell isolation

617 Wild-type (WT) C57BL/6 mice and WASP knockout (WKO) mice on the C57BL/6 background

618 were purchased from Jackson Laboratories. C56BL/6 mice expressing LifeAct-GFP transgene

619 (Riedl *et al.* 2010) were kindly provided by Dr. Roberto Weigert at National Cancer Institute,

620 USA. C56BL/6 mice expressing the LifeAct-RFP transgene were kindly provided by Dr. Klaus

621   Ley at La Jolla Institute for Allergy & Immunology. C57BL/6 mice expressing the GFP-non-

622   muscle myosin IIA (NMIIA) transgene were kindly provided by Dr. Robert Adelstein at the

623   National Heart, Lung, and Blood Institute, USA. WKO mice were bred with LifeAct-GFP mice to

624   obtain LifeAct-GFP-expressing WKO mice. GFP-NMIIA mice were crossed with LifeAct-RFP

625   mice to generate mice expressing both transgenes. N-WASP$^{flox/flox}$ on a 129Sv background

626   (Cotta-de-Almeida *et al.* 2007) were kindly provided by Dr. Lisa Westerberg at Karolinska

627   Institute, Sweden. B-cell-specific N-WASP knockout mice (cNKO, CD19$^{Cre/+}$N-WASP$^{flox/flox}$) and

628   floxed littermate controls (N-WASP$^{flox/flox}$) were obtained by breeding N-WASP$^{flox/flox}$ mice with

629   CD19$^{Cre/+}$ mice on a C57BL/6 background.

630

631   Primary B-cells were isolated from the spleens of 6 to 18 week-old male or female mice, using a

632   previously published protocol (Sharma *et al.* 2009). Briefly, mononuclear cells were isolated by

633   Ficoll density-gradient centrifugation (Millipore Sigma), and T-cells were eliminated by

634   complement-mediated cytolysis with anti-mouse CD90.2 mAb (BD Biosciences) and guinea pig

635   complement (Innovative Research Inc). Monocytes and dendritic cells were eliminated by

636   panning at 37°C and 5% CO_2. Isolated B-cells were kept on ice in DMEM (Lonza) supplemented

637   with 0.6% BSA (Thermo Fisher Scientific). All work involving mice was approved by the

638   Institutional Animal Care and Usage Committee of the University of Maryland.

639

640   **Pseudo-antigen-coated planar lipid bilayers**

641   Planar lipid bilayers (PLB) were prepared using a previously described method (Dustin *et al.*

642   2007; Liu *et al.* 2012a). Briefly, liposomes were generated from a mixture of 5 mM (total

643   concentration) 1,2-dioleoyl-sn-glycero-3-phosphocholine and 1,2-dioleoyl-sn-glycero-3-

644   phosphoethanolamine-cap-biotin (Avanti Polar Lipids) at a 100:1 molar ratio by sonication.

645   Glass coverslips, cleaned overnight with Piranha solution (KMG chemicals), were attached to 8-

646   well chambers (Lab-Tek) and incubated with liposomes (0.05 mM) in PBS for 20 min at room

647   temperature and washed with PBS. The chambers were then incubated with 1 µg/ml

648   streptavidin (Jackson ImmunoResearch Laboratories) for 10 min, washed with PBS, and then

649   incubated with 10 µg/ml mono-biotinylated Fab' fragment of goat anti-mouse Ig(G+M) (pseudo-

650   antigen) (Fab'-PLB) for 10 min, followed by PBS wash. For transferrin-coated PLB (Tf-PLB), 16

651   16 µg/ml biotinylated holoTF was used. To visualize Fab' clustering, a mixture of 0.5 µg/ml

652   Alexa Fluor (AF) 546-labeled and 9.5 µg/ml unlabeled mono-biotinylated Fab' fragment of goat

653   anti-mouse Ig(G+M) was used. The lateral mobility of AF546-Fab' on the PLB was tested using

654   fluorescence recovery after photobleaching (FRAP) to ensure ≥85% AF546 fluorescence

655   recovery within 1 min after photobleaching using a Zeiss LSM 710 equipped with a 60X oil-

656   immersion objective.

657

658   Mono-biotinylated Fab' fragments were generated as previously described (Liu *et al.* 2011).

659   Briefly, the disulfide bond linking the two Fab fragments of $F(ab')_2$ goat anti-mouse Ig(G+M) was

660   reduced using 2-mercaptoethylamine HCL (Thermo Fisher Scientific) and biotinylated by using

661   maleimide-PEG_2-biotin (Thermo Fisher Scientific). Mono-biotinylated Fab' fragments of goat

662   anti-mouse Ig(G+M) were labeled with AF546 using an Alexa Fluor 546 antibody labeling kit

663   (Thermo Fisher Scientific). The molar ratio of AF546 to Fab' in the AF546-labeled Fab' was ~2

664   determined by a Nanodrop spectrophotometer (Nanodrop Technologies).

665

666   **Total internal fluorescence microscopy**

667   To visualize molecules proximal to interacting sites between B-cells and Fab'- or Tf-PLB, we

668   utilized total internal reflection fluorescence microscopy (TIRF) and interference reflection

669   microscopy (IRM). Images were acquired using a Nikon TIRF system on an inverted microscope

670   (Nikon TE2000-PFS, Nikon Instruments Inc.) equipped with a 60X, NA 1.49 Apochromat TIRF

671   objective (Nikon), a Coolsnap HQ2 CCD camera (Roper Scientific), and two solid-state lasers of

672   wavelength 491 and 561 nm. IRM, AF488, and AF546 images were acquired sequentially.

28

673

674 The plasma membrane area of B-cells contacting PLB was determined using IRM images and

675 custom MATLAB codes. Whether a B-cell contracted or not was determined using the area

676 versus time plots, wherein if a B-cell's contact zone area reduced by $\geq$5% for at least 10 sec

677 after reaching a maximum value, it was classified as contracting. To image intracellular

678 molecules, B-cells were incubated with Fab'-PLBs for varying lengths of time in PBS at 37°C,

679 fixed with 4% paraformaldehyde, permeabilized with 0.05% saponin, and stained for various

680 molecules. For live-cell imaging, B-cells were pre-warmed to 37°C and imaged as soon as B-

681 cells were dropped into coverslip chambers coated with Fab'-PLB containing PBS in a humidity

682 chamber at 37°C, at 2 sec per frame, up to 7 min. All images from multiple independent

683 experiments were analyzed using NIH ImageJ and custom MatLab codes. Acquired

684 fluorescence intensity (FI) data were normalized to the one with the lowest FI.

685

686 **Inhibitors**

687 CK-666 (50 µM, Millipore Sigma) was used to perturb Arp2/3 activity (Nolen *et al.* 2009), and its

688 non-functional derivative CK-689 (50 µM, Millipore Sigma) as a control. CK-666 or CK-689 was

689 added at either 0 min, the start of incubation with Fab'-PLB, or at 2 min when most B-cells

690 reached maximum spreading. Notably, B-cells take approximately 1 to 1.5 min to land on PLB.

691 The time when B-cells were added to Fab'-PLB is referred to as 0 min, and the time when B-

692 cells landed on PLB as the start of spreading. The effectiveness of CK-666 was determined by

693 its inhibitory effects on the recruitment of Arp2/3, stained by an anti-Arp2 antibody (Abcam), to

694 the B-cell contact zone using TIRF (*Figure 1-figure supplement 2*). Wiskostatin (Wisko, 10 µM,

695 Millipore Sigma) was used to perturb N-WASP activity in B-cells (Peterson *et al.* 2004), with

696 DMSO used as a vehicle control. Splenic B-cells were pretreated with Wisko for 10 min at 37°C

697 before and during incubation with Fab'-PLB. The effectiveness of Wisko was determined by its

29

698   inhibitory effects on the level of phosphorylated N-WASP in the B-cell contact zone using

699   immunostaining and TIRF (*Figure 1-figure supplement 4A and C)*. Possible effects of Wisko on

700   WASP activation were evaluated by measuring the mean fluorescence intensity (MFI) of

701   phosphorylated WASP in the contact zone of B-cells treated with or without Wisko for 10 min

702   (*Figure 1-figure supplement 4B and D*).

703

704   **Analysis of the actin cytoskeleton**

705   F-actin was visualized by phalloidin staining in fixed cells and by LifeAct-GFP or LifeAct-RFP

706   expressed by primary B-cells from transgenic mice in live cells. Inner F-actin foci, visualized by

707   both phalloidin staining and LifeAct-GFP, were identified using NIH ImageJ based on the

708   following three criteria: 1) $\geq$250 nm in diameter, 2) peak fluorescence intensity (FI) $\geq$2 fold higher

709   than the FI of a nearby area containing no foci, and 3) $\geq$1 µm away from the outer edge of the B-

710   cell contact zone. The horizontal or vertical length of a focus was measured, and the lesser of

711   the two values was used as its diameter. To analyze the spatiotemporal relationship between

712   inner F-actin foci and the lamellipodial F-actin network, we generated 8 radially and equally

713   spaced kymographs from each cell using time-lapse images and MATLAB. Each kymograph

714   was either classified as contracting or not contracting based on the movement of the leading

715   edge of the B-cell contact zone. The percentage of 8 kymographs from each cell exhibiting inner

716   F-actin foci that could be traced back to lamellipodial F-actin when the B-cell switched from

717   spreading to contraction was determined.

718   The relative speeds and lifetimes of F-actin foci were determined using three randomly

719   positioned kymographs from each B-cell and F-actin focuses emerging during a 60-sec window

720   right after B-cell maximal spreading. Only those remaining visible in individual kymographs for at

721   least 4 sec were analyzed. The time duration of each F-actin foci detected in a kymograph was

722   used to determine the relative lifetime. The distances individual F-actin foci moved during their

723   lifetimes were used to determine the relative speed. The term 'relative' has been used because

724 the disappearance of an F-actin focus could be due to its movement away from the region used

725 for the kymograph or vertically from the TIRF evanescent field of excitation.

726 To determine the rate of myosin recruitment, GFP-NMIIA MFI in the B-cell contact zone was

727 plotted over time, and the slope for the initial segment of the MFI versus the time plot was

728 determined using linear regression. The percentage of B-cells with the NMIIA ring was

729 determined by visual inspection.

730

731 **Analysis of BCR-Fab' clusters**

732 BCR clusters were identified by clustering of AF546-Fab' on PLBs using custom code by

733 MATLAB. We utilized the median FI of the Fab'-PLB within the same area outside but near the

734 B-cell contact zone as the background. The median, but not mean FI value was used for

735 background FI calculations to minimize fluctuations due to debris. To ensure that individual

736 clusters with varying FI were detected as distinct objects, we used 16 graded thresholds from

737 1.1 to 4.1 fold of the background (0.2 fold apart) to acquire 16 sets of binary masks for each

738 frame of time-lapse images from each cell. When clusters were detected by multiple thresholds

739 at the same location, only the one identified by the highest threshold was retained. Objects that

740 were smaller than 250 nm in diameter or could not be tracked for at least 20 sec were

741 eliminated. This allowed us to detect the position of BCR-Fab' clusters and track them over time

742 until they merged with other clusters. The horizontal or vertical length of a focus was measured,

743 and the lesser of the two values was used as its diameter. We chose the peak FI as a metric for

744 the extent of Fab' clustering by the BCR, because it does not rely on the area occupied by each

745 cluster. The rate of peak FI increase was determined by linear regression of peak FI versus time

746 curves for each cluster for a given window of time.

747

748 **BCR signaling**

749   Splenic B-cells were incubated with AF546-Fab'-PLB at 37ºC and fixed at 1, 3, 5, 7, and 9 min.

750   After fixation, cells were stained for phosphorylated CD79a (pCD79a, Y182) (Cell Signaling

751   Technology), Syk (pSyk, Y519/520) (Cell Signaling Technology), SHIP-1 (pSHIP-1, Y1020) (Cell

752   Signaling Technology), or total Syk or SHIP-1 proteins (Thermo Fisher Scientific). We identified

753   BCR-Fab' clusters as described. We determined the peak FI of AF546-Fab' and the MFI of

754   AF546-Fab', pCD79a, pSyk, pSHIP-1, Syk, or SHIP-1 within each cluster. The ratio of pCD79a

755   MFI to AF546-Fab' MFI in the same cluster was used to estimate the relative phosphorylation

756   level of BCRs in that cluster. This MFI ratio was plotted against AF546-Fab' peak FI to analyze

757   the relationship between BCR phosphorylation and BCR density of individual clusters. We

758   calculated the MFI ratio of Syk to Fab' or SHIP-1 to Fab' in individual clusters to estimate the

759   relative recruitment level of Syk or SHIP-1 to BCR clusters. We plotted these MFI ratios against

760   Fab' peak FI to determine the relationship between Syk and SHIP-1 recruitment levels and BCR

761   density in individual clusters. We calculated the MFI ratio of pSyk to Fab' or pSHIP-1 to Fab' to

762   estimate the amount of pSyk or pSHIP-1 relative to BCR in individual clusters. We plotted these

763   MFI ratios against Fab' peak FI to determine the relationship between Syk or SHIP-1

764   phosphorylation and BCR density in individual clusters. We identified pSyk or pSHIP-1 puncta

765   using the criteria: ≥1.3 fold of the background staining outside the B-cell contact zone and ≥250

766   nm in diameter. We calculated the MFI ratio of pSyk to Fab' or pSHIP-1 to Fab' in individual

767   puncta to estimate the amount of pSyk or pSHIP-1 relative to BCR in individual puncta. We

768   plotted these MFI ratios against Fab' peak FI to determine the relationship between Syk or

769   SHIP-1 phosphorylation and BCR density in individual puncta.

770

771   **Statistical analysis**

772   Statistical analysis was performed using the Mann-Whitney U non-parametric test for unpaired

773   groups having different sample sizes or the Student's *t*-test for paired groups with the same

774   sample size. To compare curves, Kolmogorov-Smirnov test was used. Statistical analyses were

32

775   performed in Microsoft Excel, GraphPad Prism, and MATLAB. All data are presented as mean ±

776   SEM (standard error of the mean). When testing multiple hypotheses, *p*--values acquired using

777   t-tests were corrected using the Benjamini-Hochberg/Yekutieli method for false discovery rate

778   control.

779

780   **MATLAB scripts**

781   All MATLAB scripts used for this study are available as supplemental materials.

782

783   **Acknowledgements**

789

790   **References**

791   Adachi, T., Wienands, J., Wakabayashi, C., Yakura, H., Reth, M. and Tsubata, T. (2001) 'SHP-1
792   requires inhibitory co-receptors to down-modulate B cell antigen receptor-mediated
793   phosphorylation of cellular substrates', *J Biol Chem*, 276(28), 26648-55, available:
794   http://dx.doi.org/10.1074/jbc.M100997200.

795
796   Aman, M.J., Lamkin, T.D., Okada, H., Kurosaki, T. and Ravichandran, K.S. (1998) 'The inositol
797   phosphatase SHIP inhibits Akt/PKB activation in B cells', *J Biol Chem*, 273(51), 33922-8,
798   available: http://dx.doi.org/10.1074/jbc.273.51.33922.

799
800   Batista, F.D. and Harwood, N.E. (2009) 'The who, how and where of antigen presentation to B
801   cells', *Nat Rev Immunol*, 9(1), 15-27, available: http://dx.doi.org/10.1038/nri2454.

802
803   Batista, F.D., Treanor, B. and Harwood, N.E. (2010) 'Visualizing a role for the actin cytoskeleton
804   in the regulation of B-cell activation', *Immunol Rev*, 237(1), 191-204, available:
805   http://dx.doi.org/10.1111/j.1600-065X.2010.00943.x.

806

807 Bolger-Munro, M., Choi, K., Scurll, J.M., Abraham, L., Chappell, R.S., Sheen, D., Dang-Lawson,
808   M., Wu, X., Priatel, J.J., Coombs, D., Hammer, J.A. and Gold, M.R. (2019) 'Arp2/3
809   complex-driven spatial patterning of the BCR enhances immune synapse formation,
810   BCR signaling and B cell activation', *Elife*, 8, available:
811   http://dx.doi.org/10.7554/eLife.44574.

812

813 Bolland, S., Pearse, R.N., Kurosaki, T. and Ravetch, J.V. (1998) 'SHIP modulates immune
814   receptor responses by regulating membrane association of Btk', *Immunity*, 8(4), 509-16,
815   available: http://dx.doi.org/10.1016/s1074-7613(00)80555-5.

816

817 Brauweiler, A.M., Tamir, I. and Cambier, J.C. (2000) 'Bilevel control of B-cell activation by the
818   inositol 5-phosphatase SHIP', *Immunol Rev*, 176, 69-74.

819

820 Bunnell, S.C., Kapoor, V., Trible, R.P., Zhang, W. and Samelson, L.E. (2001) 'Dynamic actin
821   polymerization drives T cell receptor-induced spreading: a role for the signal
822   transduction adaptor LAT', *Immunity*, 14(3), 315-29, available:
823   http://dx.doi.org/10.1016/s1074-7613(01)00112-1.

824

825 Carrasco, Y.R., Fleire, S.J., Cameron, T., Dustin, M.L. and Batista, F.D. (2004) 'LFA-1/ICAM-1
826   interaction lowers the threshold of B cell activation by facilitating B cell adhesion and
827   synapse formation', *Immunity*, 20(5), 589-99.

828

829 Cotta-de-Almeida, V., Westerberg, L., Maillard, M.H., Onaldi, D., Wachtel, H., Meelu, P., Chung,
830   U.I., Xavier, R., Alt, F.W. and Snapper, S.B. (2007) 'Wiskott Aldrich syndrome protein
831   (WASP) and N-WASP are critical for T cell development', *Proc Natl Acad Sci U S A*,
832   104(39), 15424-9, available: http://dx.doi.org/10.1073/pnas.0706881104.

833

834 Cyster, J.G. (2010) 'B cell follicles and antigen encounters of the third kind', *Nat Immunol*,
835   11(11), 989-96, available: http://dx.doi.org/10.1038/ni.1946.

836

837 Dal Porto, J.M., Gauld, S.B., Merrell, K.T., Mills, D., Pugh-Bernard, A.E. and Cambier, J. (2004)
838   'B cell antigen receptor signaling 101', *Mol Immunol*, 41(6-7), 599-613, available:
839   http://dx.doi.org/10.1016/j.molimm.2004.04.008.

840

841 Depoil, D., Weber, M., Treanor, B., Fleire, S.J., Carrasco, Y.R., Harwood, N.E. and Batista, F.D.
842   (2009) 'Early events of B cell activation by antigen', *Sci Signal*, 2(63), pt1, available:
843   http://dx.doi.org/10.1126/scisignal.263pt1.

844

845 Dong, Y., Pi, X., Bartels-Burgahn, F., Saltukoglu, D., Liang, Z., Yang, J., Alt, F.W., Reth, M. and
846   Wu, H. (2022) 'Structural principles of B cell antigen receptor assembly', *Nature*,
847   612(7938), 156-161, available: http://dx.doi.org/10.1038/s41586-022-05412-7.

848

849   Dustin, M.L., Starr, T., Varma, R. and Thomas, V.K. (2007) 'Supported planar bilayers for study
850   of the immunological synapse', *Curr Protoc Immunol*, Chapter 18, Unit 18.13, available:
851   http://dx.doi.org/10.1002/0471142735.im1813s76.

853   Fenix, A.M. and Burnette, D.T. (2018) 'Assembly of myosin II filament arrays: Network
854   Contraction versus Expansion', *Cytoskeleton (Hoboken)*, 75(12), 545-549, available:
855   http://dx.doi.org/10.1002/cm.21487.

857   Fleire, S.J., Goldman, J.P., Carrasco, Y.R., Weber, M., Bray, D. and Batista, F.D. (2006) 'B cell
858   ligand discrimination through a spreading and contraction response', *Science*,
859   312(5774), 738-41, available: http://dx.doi.org/10.1126/science.1123940.

861   Franks, S.E. and Cambier, J.C. (2018) 'Putting on the Brakes: Regulatory Kinases and
862   Phosphatases Maintaining B Cell Anergy', *Front Immunol*, 9, 665, available:
863   http://dx.doi.org/10.3389/fimmu.2018.00665.

865   Freeman, S.A., Lei, V., Dang-Lawson, M., Mizuno, K., Roskelley, C.D. and Gold, M.R. (2011)
866   'Cofilin-mediated F-actin severing is regulated by the Rap GTPase and controls the
867   cytoskeletal dynamics that drive lymphocyte spreading and BCR microcluster formation',
868   *J Immunol*, 187(11), 5887-900, available: http://dx.doi.org/10.4049/jimmunol.1102233.

870   Gitlin, A.D., Shulman, Z. and Nussenzweig, M.C. (2014) 'Clonal selection in the germinal centre
871   by regulated proliferation and hypermutation', *Nature*, 509(7502), 637-40, available:
872   http://dx.doi.org/10.1038/nature13300.

874   Gonzalez, S.F., Pitcher, L.A., Mempel, T., Schuerpf, F. and Carroll, M.C. (2009) 'B cell
875   acquisition of antigen in vivo', *Curr Opin Immunol*, 21(3), 251-7, available:
876   http://dx.doi.org/10.1016/j.coi.2009.05.013.

878   Gross, A.J., Lyandres, J.R., Panigrahi, A.K., Prak, E.T. and DeFranco, A.L. (2009)
879   'Developmental acquisition of the Lyn-CD22-SHP-1 inhibitory pathway promotes B cell
880   tolerance', *J Immunol*, 182(9), 5382-92, available:
881   http://dx.doi.org/10.4049/jimmunol.0803941.

883   Hammer, J.A., Wang, J.C., Saeed, M. and Pedrosa, A.T. (2019) 'Origin, Organization,
884   Dynamics, and Function of Actin and Actomyosin Networks at the T Cell Immunological
885   Synapse', *Annu Rev Immunol*, 37, 201-224, available: http://dx.doi.org/10.1146/annurev-
886   immunol-042718-041341.

888   Harwood, N.E. and Batista, F.D. (2010) 'Early events in B cell activation', *Annu Rev Immunol*,
889   28, 185-210, available: http://dx.doi.org/10.1146/annurev-immunol-030409-101216.

890

891 Harwood, N.E. and Batista, F.D. (2011) 'The cytoskeleton coordinates the early events of B-cell
892   activation', *Cold Spring Harb Perspect Biol*, 3(2), available:
893   http://dx.doi.org/10.1101/cshperspect.a002360.

895 Hoogeboom, R., Natkanski, E.M., Nowosad, C.R., Malinova, D., Menon, R.P., Casal, A. and
896   Tolar, P. (2018) 'Myosin IIa Promotes Antibody Responses by Regulating B Cell
897   Activation, Acquisition of Antigen, and Proliferation', *Cell Rep*, 23(8), 2342-2353,
898   available: http://dx.doi.org/10.1016/j.celrep.2018.04.087.

900 Hoogeboom, R. and Tolar, P. (2016) 'Molecular Mechanisms of B Cell Antigen Gathering and
901   Endocytosis', *Curr Top Microbiol Immunol*, 393, 45-63, available:
902   http://dx.doi.org/10.1007/82_2015_476.

904 Kinnon, C., Hinshelwood, S., Levinsky, R.J. and Lovering, R.C. (1993) 'X-linked
905   agammaglobulinemia--gene cloning and future prospects', *Immunol Today*, 14(11), 554-
906   8, available: http://dx.doi.org/10.1016/0167-5699(93)90187-P.

908 Kläsener, K., Maity, P.C., Hobeika, E., Yang, J. and Reth, M. (2014) 'B cell activation involves
909   nanoscale receptor reorganizations and inside-out signaling by Syk', *Elife*, 3, e02069.

911 Koestler, S.A., Auinger, S., Vinzenz, M., Rottner, K. and Small, J.V. (2008) 'Differentially
912   oriented populations of actin filaments generated in lamellipodia collaborate in pushing
913   and pausing at the cell front', *Nat Cell Biol*, 10(3), 306-13, available:
914   http://dx.doi.org/10.1038/ncb1692.

916 Krause, M. and Gautreau, A. (2014) 'Steering cell migration: lamellipodium dynamics and the
917   regulation of directional persistence', *Nat Rev Mol Cell Biol*, 15(9), 577-90, available:
918   http://dx.doi.org/10.1038/nrm3861.

920 Kurosaki, T. (2000) 'Functional dissection of BCR signaling pathways', *Curr Opin Immunol*,
921   12(3), 276-81.

923 Kurosaki, T., Shinohara, H. and Baba, Y. (2010) 'B cell signaling and fate decision', *Annu Rev
924   Immunol*, 28, 21-55, available:
925   http://dx.doi.org/10.1146/annurev.immunol.021908.132541.

927 Kwak, K., Akkaya, M. and Pierce, S.K. (2019) 'B cell signaling in context', *Nat Immunol*, 20(8),
928   963-969, available: http://dx.doi.org/10.1038/s41590-019-0427-9.

930 Leung, W.H., Tarasenko, T., Biesova, Z., Kole, H., Walsh, E.R. and Bolland, S. (2013) 'Aberrant
931   antibody affinity selection in SHIP-deficient B cells', *Eur J Immunol*, 43(2), 371-81,
932   available: http://dx.doi.org/10.1002/eji.201242809.

934 Levayer, R. and Lecuit, T. (2012) 'Biomechanical regulation of contractility: spatial control and
935   dynamics', *Trends Cell Biol*, 22(2), 61-81, available:
936   http://dx.doi.org/10.1016/j.tcb.2011.10.001.

938 Liu, C., Bai, X., Wu, J., Sharma, S., Upadhyaya, A., Dahlberg, C.I., Westerberg, L.S., Snapper,
939   S.B., Zhao, X. and Song, W. (2013a) 'N-WASP is essential for the negative regulation of
940   B cell receptor signaling', *PLoS Biol*, 11(11), e1001704, available:
941   http://dx.doi.org/10.1371/journal.pbio.1001704.

943 Liu, C., Fallen, M.K., Miller, H., Upadhyaya, A. and Song, W. (2013b) 'The actin cytoskeleton
944   coordinates the signal transduction and antigen processing functions of the B cell
945   antigen receptor', *Front Biol (Beijing)*, 8(5), 475-485, available:
946   http://dx.doi.org/10.1007/s11515-013-1272-0.

948 Liu, C., Miller, H., Hui, K.L., Grooman, B., Bolland, S., Upadhyaya, A. and Song, W. (2011) 'A
949   balance of Bruton's tyrosine kinase and SHIP activation regulates B cell receptor cluster
950   formation by controlling actin remodeling', *J Immunol*, 187(1), 230-9, available:
951   http://dx.doi.org/10.4049/jimmunol.1100157.

953 Liu, C., Miller, H., Orlowski, G., Hang, H., Upadhyaya, A. and Song, W. (2012a) 'Actin
954   reorganization is required for the formation of polarized B cell receptor signalosomes in
955   response to both soluble and membrane-associated antigens', *J Immunol*, 188(7), 3237-
956   46, available: http://dx.doi.org/10.4049/jimmunol.1103065.

958 Liu, C., Miller, H., Sharma, S., Beaven, A., Upadhyaya, A. and Song, W. (2012b) 'Analyzing
959   actin dynamics during the activation of the B cell receptor in live B cells', *Biochem
960   Biophys Res Commun*, 427(1), 202-6, available:
961   http://dx.doi.org/10.1016/j.bbrc.2012.09.046.

963 Maeda, F.Y., van Haaren, J.J., Langley, D.B., Christ, D., Andrews, N.W. and Song, W. (2021)
964   'Surface-associated antigen induces permeabilization of primary mouse B-cells and
965   lysosome exocytosis facilitating antigen uptake and presentation to T-cells', *Elife*, 10,
966   available: http://dx.doi.org/10.7554/eLife.66984.

968 Matsumura, F. (2005) 'Regulation of myosin II during cytokinesis in higher eukaryotes', *Trends
969   Cell Biol*, 15(7), 371-7, available: http://dx.doi.org/10.1016/j.tcb.2005.05.004.

971 Mizuno, K., Tagawa, Y., Mitomo, K., Arimura, Y., Hatano, N., Katagiri, T., Ogimoto, M. and
972   Yakura, H. (2000) 'Src homology region 2 (SH2) domain-containing phosphatase-1
973   dephosphorylates B cell linker protein/SH2 domain leukocyte protein of 65 kDa and
974   selectively regulates c-Jun NH2-terminal kinase activation in B cells', *J Immunol*, 165(3),
975   1344-51, available: http://dx.doi.org/10.4049/jimmunol.165.3.1344.

976

977   Natkanski, E., Lee, W.Y., Mistry, B., Casal, A., Molloy, J.E. and Tolar, P. (2013) 'B cells use
978   mechanical energy to discriminate antigen affinities', *Science*, 340(6140), 1587-90,
979   available: http://dx.doi.org/10.1126/science.1237572.

980
981   Nolen, B.J., Tomasevic, N., Russell, A., Pierce, D.W., Jia, Z., McCormick, C.D., Hartman, J.,
982   Sakowicz, R. and Pollard, T.D. (2009) 'Characterization of two classes of small molecule
983   inhibitors of Arp2/3 complex', *Nature*, 460(7258), 1031-4, available:
984   http://dx.doi.org/10.1038/nature08231.

985
986   Padrick, S.B. and Rosen, M.K. (2010) 'Physical mechanisms of signal integration by WASP
987   family proteins', *Annu Rev Biochem*, 79, 707-35, available:
988   http://dx.doi.org/10.1146/annurev.biochem.77.060407.135452.

989
990   Pao, L.I., Lam, K.P., Henderson, J.M., Kutok, J.L., Alimzhanov, M., Nitschke, L., Thomas, M.L.,
991   Neel, B.G. and Rajewsky, K. (2007) 'B cell-specific deletion of protein-tyrosine
992   phosphatase Shp1 promotes B-1a cell development and causes systemic autoimmunity',
993   *Immunity*, 27(1), 35-48, available: http://dx.doi.org/10.1016/j.immuni.2007.04.016.

994
995   Peterson, J.R., Bickford, L.C., Morgan, D., Kim, A.S., Ouerfelli, O., Kirschner, M.W. and Rosen,
996   M.K. (2004) 'Chemical inhibition of N-WASP by stabilization of a native autoinhibited
997   conformation', *Nat Struct Mol Biol*, 11(8), 747-55, available:
998   http://dx.doi.org/10.1038/nsmb796.

999
1000 Pierce, S.K. (2002) 'Lipid rafts and B-cell activation', *Nat Rev Immunol*, 2(2), 96-105, available:
1001   http://dx.doi.org/10.1038/nri726.

1002
1003 Reth, M. (1994) 'B cell antigen receptors', *Curr Opin Immunol*, 6(1), 3-8.

1004
1005 Reth, M. and Wienands, J. (1997) 'Initiation and processing of signals from the B cell antigen
1006   receptor', *Annu Rev Immunol*, 15, 453-79, available:
1007   http://dx.doi.org/10.1146/annurev.immunol.15.1.453.

1008
1009 Rey-Suarez, I., Wheatley, B.A., Koo, P., Bhanja, A., Shu, Z., Mochrie, S., Song, W., Shroff, H.
1010   and Upadhyaya, A. (2020) 'WASP family proteins regulate the mobility of the B cell
1011   receptor during signaling activation', *Nat Commun*, 11(1), 439, available:
1012   http://dx.doi.org/10.1038/s41467-020-14335-8.

1013
1014 Riedl, J., Flynn, K.C., Raducanu, A., Gärtner, F., Beck, G., Bösl, M., Bradke, F., Massberg, S.,
1015   Aszodi, A., Sixt, M. and Wedlich-Söldner, R. (2010) 'Lifeact mice for studying F-actin
1016   dynamics', *Nat Methods*, 7(3), 168-9, available: http://dx.doi.org/10.1038/nmeth0310-
1017   168.

1018

Rotty, J.D., Wu, C. and Bear, J.E. (2013) 'New insights into the regulation and cellular functions of the ARP2/3 complex', *Nat Rev Mol Cell Biol*, 14(1), 7-12, available: http://dx.doi.org/10.1038/nrm3492.

Schreiner, G.F. and Unanue, E.R. (1977) 'Capping and the lymphocyte: models for membrane reorganization', *J Immunol*, 119(5), 1549-51.

Seeley-Fallen, M.K., Lazzaro, M., Liu, C., Li, Q.Z., Upadhyaya, A. and Song, W. (2022) 'Non-Muscle Myosin II Is Essential for the Negative Regulation of B-Cell Receptor Signaling and B-Cell Activation', *Front Immunol*, 13, 842605, available: http://dx.doi.org/10.3389/fimmu.2022.842605.

Seeley-Fallen, M.K., Liu, L.J., Shapiro, M.R., Onabajo, O.O., Palaniyandi, S., Zhu, X., Tan, T.H., Upadhyaya, A. and Song, W. (2014) 'Actin-binding protein 1 links B-cell antigen receptors to negative signaling pathways', *Proc Natl Acad Sci U S A*, 111(27), 9881-6, available: http://dx.doi.org/10.1073/pnas.1321971111.

Sharma, S., Orlowski, G. and Song, W. (2009) 'Btk regulates B cell receptor-mediated antigen processing and presentation by controlling actin cytoskeleton dynamics in B cells', *J Immunol*, 182(1), 329-39.

Shen, Z., Liu, S., Li, X., Wan, Z., Mao, Y., Chen, C. and Liu, W. (2019) 'Conformational change within the extracellular domain of B cell receptor in B cell activation upon antigen binding', *Elife*, 8, available: http://dx.doi.org/10.7554/eLife.42271.

Shlomchik, M.J., Luo, W. and Weisel, F. (2019) 'Linking signaling and selection in the germinal center', *Immunol Rev*, 288(1), 49-63, available: http://dx.doi.org/10.1111/imr.12744.

Skau, C.T. and Waterman, C.M. (2015) 'Specification of Architecture and Function of Actin Structures by Actin Nucleation Factors', *Annu Rev Biophys*, 44, 285-310, available: http://dx.doi.org/10.1146/annurev-biophys-060414-034308.

Sohn, H.W., Tolar, P. and Pierce, S.K. (2008) 'Membrane heterogeneities in the formation of B cell receptor-Lyn kinase microclusters and the immune synapse', *J Cell Biol*, 182(2), 367-79, available: http://dx.doi.org/10.1083/jcb.200802007.

Song, W., Cho, H., Cheng, P. and Pierce, S.K. (1995) 'Entry of B cell antigen receptor and antigen into class II peptide-loading compartment is independent of receptor cross-linking', *J Immunol*, 155(9), 4255-63.

Song, W., Liu, C., Seeley-Fallen, M.K., Miller, H., Ketchum, C. and Upadhyaya, A. (2013) 'Actin-mediated feedback loops in B-cell receptor signaling', *Immunol Rev*, 256(1), 177-89, available: http://dx.doi.org/10.1111/imr.12113.

Su, Q., Chen, M., Shi, Y., Zhang, X., Huang, G., Huang, B., Liu, D. and Liu, Z. (2022) 'Cryo-EM structure of the human IgM B cell receptor', *Science*, 377(6608), 875-880, available: http://dx.doi.org/10.1126/science.abo3923.

Tanaka, S. and Baba, Y. (2020) 'B Cell Receptor Signaling', *Adv Exp Med Biol*, 1254, 23-36, available: http://dx.doi.org/10.1007/978-981-15-3532-1_2.

Tojkander, S., Gateva, G., Husain, A., Krishnan, R. and Lappalainen, P. (2015) 'Generation of contractile actomyosin bundles depends on mechanosensitive actin filament assembly and disassembly', *Elife*, 4, e06126, available: http://dx.doi.org/10.7554/eLife.06126.

Tolar, P., Hanna, J., Krueger, P.D. and Pierce, S.K. (2009a) 'The constant region of the membrane immunoglobulin mediates B cell-receptor clustering and signaling in response to membrane antigens', *Immunity*, 30(1), 44-55, available: http://dx.doi.org/10.1016/j.immuni.2008.11.007.

Tolar, P., Sohn, H.W., Liu, W. and Pierce, S.K. (2009b) 'The molecular assembly and organization of signaling active B-cell receptor oligomers', *Immunol Rev*, 232(1), 34-41, available: http://dx.doi.org/10.1111/j.1600-065X.2009.00833.x.

Tolar, P., Sohn, H.W. and Pierce, S.K. (2005) 'The initiation of antigen-induced B cell antigen receptor signaling viewed in living cells by fluorescence resonance energy transfer', *Nat Immunol*, 6(11), 1168-76, available: http://dx.doi.org/10.1038/ni1262.

Treanor, B., Depoil, D., Gonzalez-Granja, A., Barral, P., Weber, M., Dushek, O., Bruckbauer, A. and Batista, F.D. (2010) 'The membrane skeleton controls diffusion dynamics and signaling through the B cell receptor', *Immunity*, 32(2), 187-99, available: http://dx.doi.org/10.1016/j.immuni.2009.12.005.

Unanue, E.R. and Karnovsky, M.J. (1973) 'Redistribution and fate of Ig complexes on surface of B lymphocytes: functional implications and mechanisms', *Transplant Rev*, 14, 184-210, available: http://dx.doi.org/10.1111/j.1600-065x.1973.tb00107.x.

Vicente-Manzanares, M., Ma, X., Adelstein, R.S. and Horwitz, A.R. (2009) 'Non-muscle myosin II takes centre stage in cell adhesion and migration', *Nat Rev Mol Cell Biol*, 10(11), 778-90, available: http://dx.doi.org/10.1038/nrm2786.

Wang, H., Morse, H.C. and Bolland, S. (2020) 'Transcriptional Control of Mature B Cell Fates', *Trends Immunol*, 41(7), 601-613, available: http://dx.doi.org/10.1016/j.it.2020.04.011.

Wang, J.C., Yim, Y.I., Wu, X., Jaumouille, V., Cameron, A., Waterman, C.M., Kehrl, J.H. and Hammer, J.A. (2022) 'A B-cell actomyosin arc network couples integrin co-stimulation to mechanical force-dependent immune synapse formation', *Elife*, 11, available: http://dx.doi.org/10.7554/eLife.72805.

1107
1108   Westerberg, L.S., Dahlberg, C., Baptista, M., Moran, C.J., Detre, C., Keszei, M., Eston, M.A.,
1109   Alt, F.W., Terhorst, C., Notarangelo, L.D. and Snapper, S.B. (2012) 'Wiskott-Aldrich
1110   syndrome protein (WASP) and N-WASP are critical for peripheral B-cell development
1111   and function', *Blood*, 119(17), 3966-74, available: http://dx.doi.org/10.1182/blood-2010-
1112   09-308197.

1113
1114   Yang, J. and Reth, M. (2010) 'Oligomeric organization of the B-cell antigen receptor on resting
1115   cells', *Nature*, 467(7314), 465-9, available: http://dx.doi.org/10.1038/nature09357.

1116

1117

Figure legend

Figure 1. Arp2/3, activated by N-WASP but not WASP, is required for B-cell contraction.

Splenic B-cells were incubated with planar lipid bilayers coated with monobiotinylated Fab'

fragment of goat anti-mouse IgG+M (Fab'-PLB) in the absence and presence of various

inhibitors and imaged live at 37°C by interference reflection microscopy (IRM). The B-cell

plasma membrane area contacting Fab'-PLB (B-cell contact zone) was measured using IRM

images and custom MATLAB scripts. (**A**) Representative IRM images of splenic B-cells from

C57BL/6 mice treated with CK-689 or CK-666 (50 µM) before (0 min) and after maximal

spreading (2 min). (**B**) Representative plots of the B-cell contact area versus time from one

contracting cell and one non-contracting cell. (**C**) Percentages (±SEM) of B-cells that underwent

contraction after treatment with CK-666 or CK-689. (**D**) Representative IRM images of splenic

B-cells from C57BL/6 mice treated with DMSO or Wiskostatin (Wisko, 10 µM) 10 min before and

during incubation with Fab'-PLB. (**E**) Percentages (±SEM) of B-cells that underwent contraction

after treatment with Wisko or DMSO. (**F**) Representative IRM images of splenic B-cells from flox

control and B-cell-specific N-WASP knockout (cNKO) mice. (**G**) Percentages (±SEM) of cNKO

or flox control B-cells that underwent contraction. (**H**) Representative IRM images of splenic B-

cells from WT or WASP knockout mice (WKO). (**I**) Percentages (±SEM) of WKO or WT B-cells

that underwent contraction. Data were generated from three independent experiments, with ~25

cells per condition, per experiment. Scale bar, 2 µm. *p <0.05, ***p<0.001, by paired student's t-

test.

Figure supplement 1. B-cells spread and contract on Fab'-coated-planar lipid bilayers.

Figure supplement 2. CK-666 significantly decreases Arp2/3 recruitment to the B-cell contact

zone.

Figure supplement 3. CK-666 treatment before but not after maximal B-cell spreading

decreases the spreading kinetics.

1143 **Figure supplement 4.** Wiskostatin treatment inhibits N-WASP activation while enhancing

1144 WASP activation in B-cells.

1145 **Figure 1–Video 1.** Effects of CK-666, Wiskostatin, conditional N-WASP knockout, and WASP

1146 knockout on B-cell contraction.

1147

1148 **Figure 2. Arp2/3, downstream of N-WASP, generates inner F-actin foci, driving B-cell**

1149 **contraction.** (**A-C**) WT splenic B-cells were treated with CK-689 or CK-666 (50 μM) during

1150 incubation with Fab'-PLB (**A and B**), and flox control and cNKO B-cells were incubated with

1151 Fab'-PLB at 37°C **(C)**. Cells were fixed at 2 and 4 min, permeabilized, stained for F-actin with

1152 phalloidin, and analyzed using TIRF. Shown are representative TIRF images of phalloidin

1153 staining in the contact zone of CK-689 and CK-666-treated B-cells (**A,** left panels) and

1154 fluorescence intensity (FI) profiles of phalloidin staining along a line crossing cells (**A,** right

1155 panels). Green arrows indicate lamellipodial F-actin, and purple arrows indicate inner F-actin

1156 foci forming a ring-like structure. Percentages of cells (per image) (±SEM) with inner F-actin foci

1157 forming ring-like distribution among CK-689- versus CK-666-treated cells (**B**) and flox control

1158 versus cNKO B-cells (**C**) before (2 min) and after (4 min) contraction were determined by visual

1159 inspection of phalloidin FI line-profiles across the B-cell contact zones. Data were generated

1160 from 3 independent experiments with 5 images per condition per experiment and ~15 cells per

1161 image. (**D-G**) Inner F-actin foci were identified by their diameter ($\geq$250 nm), peak FI ($\geq$2 fold of

1162 no foci area, and location (1 μm away from the outer edge) and quantified as the number per

1163 cell using TIRF images. (**D**) Shown are representative images of splenic B-cells from LifeAct-

1164 GFP-expressing mice treated with CK-689 or CK-666 from 0 min during incubation with Fab'-

1165 PLB at 37°C (top) and the average number (±SEM) of inner LifeAct-GFP foci per cell (bottom) at

1166 2 min. (**E**) LifeAct-GFP B-cells were treated with CK-666 at 2 min. Shown are representative

1167 TIRF images of LifeAct-GFP in the contact zone of B-cells (top) and the average number

1168 (±SEM) of inner LifeAct-GFP foci (bottom) in the same cell 10s before and 20s after CK-666

1169   treatment. (**F**) Shown are representative TIRF images of phalloidin-staining in the contact zone

1170   of flox control and cNKO B-cells after incubating with Fab'-PLB for 2 min (top) and the average

1171   number (±SEM) of inner F-actin foci per cell (bottom). (**H**) Shown are representative TIRF

1172   images of WT and WKO B-cells expressing LifeAct-GFP incubated with Fab'-PLB for 2 min and

1173   the average number (±SEM) of inner F-actin foci per cell (bottom). Data points represent

1174   individual cells from three independent experiments with 10 (**D, F, and G**) or 6 (**E**) cells per

1175   condition per experiment. Scale bar, 2 μm. ** *p* <0.01, *** *p*<0.001, by non-parametric

1176   student's *t*-test.

1177   **Figure 2-Video 1.** Effects of CK-666 and WKO on F-actin foci formation.

1178

1179   **Figure 3. Inner F-actin foci are originated from lamellipodia behind the spreading**

1180   **membrane.** Mouse splenic B-cells from LifeAct-GFP transgenic mice were treated with DMSO

1181   or Wisko (10 μM), imaged live using TIRF during incubation with Fab'-PLB at 37°C, and

1182   analyzed using kymographs generated by NIH ImageJ. (**A**) One frame of TIRF time-lapse

1183   images of LifeAct-GFP in the contact zone of B-cells treated with DMSO or Wisko. Lines

1184   indicate eight kymographs that were randomly generated from each cell. (**B**) Representative

1185   kymographs were generated from TIRF time-lapse images of LifeAct-GFP at the red line in (A).

1186   Top panel, a contracting cell. Arrows indicate the start of contraction with inner F-actin foci

1187   originating from lamellipodia. Bottom panel, a non-contracting cell. Lamellipodia-derived inner F-

1188   actin foci were identified by their LifeAct-GFP FI ≥2 fold of their nearby region, migrating out of

1189   the lamellipodial F-actin toward the center of the contact zone, and trackable for >8 sec. (**C**)

1190   Percentages (±SEM) of kymographs showing inner F-actin foci originating from lamellipodia per

1191   cell that did and did not undergo contraction. Data were generated from 3 independent

1192   experiments with ~10 cells per condition per experiment. (**D**) A histogram of inner F-actin foci

1193   emerging (expressed as percentages of the total events, blue line) over time relative to the time

1194   of B-cell contraction (defined as 0 sec, indicated by a purple dash line and arrow). Data were

44

1195   generated from 5 independent experiments with ~9 cells per condition per experiment**. (E)**

1196   Percentage (±SEM) of inner F-actin foci originated from lamellipodia observed in 8 randomly

1197   positioned kymographs of each DMSO- or Wisko-treated WT or untreated WKO B-cell. Data

1198   were generated from 3 independent experiments with ~10 cells per condition per experiment**.**

1199   Scale bars, 2 µm. *** $p<0.001$, by non-parametric student's *t*-test.

1200   **Figure supplement 1.** Emerging of Inner F-actin foci from lamellipodia.

1201

1202   **Figure 4. N-WASP-activated Arp2/3 sustains the lifetime and the centripetal movement of**

1203   **inner F-actin foci.** LifeAct-GFP-expressing B-cells were incubated with or without various

1204   inhibitors and imaged live by TIRF during interaction with Fab'-PLB at 37°C. Three randomly

1205   positioned kymographs were generated for each cell using time-lapse images. (**A**) A

1206   representative kymograph from TIRF time-lapse images of a DMSO-treated B-cell (Left panels).

1207   Inner F-actin foci were identified as described in Figure 3, and those that emerged during the 60

1208   sec window after maximal spreading (white rectangles in B) and can be tracked for ≥ 4 sec

1209   (dashed lines) in individual kymographs were analyzed. Relative lifetimes of inner F-actin foci

1210   were measured using the duration each focus could be detected in a kymograph. The relative

1211   distances traveled by the foci were measured using the displacement of each focus in a

1212   kymograph. Relative speed was calculated for each inner F-actin focus by dividing its relative

1213   distance by its relative lifetime (right panels). (**B-D**) B-cells were treated with CK-689 or CK-666

1214   (50 µM) from the beginning of the incubation with Fab'-PLB (0 min). Shown are representative

1215   kymographs (**B**), relative lifetimes (**C**), and relative speed (**D**) of inner F-actin foci in CK-689-

1216   versus CK-666-treated B-cells. (**E-G**) B-cells were treated with CK-666 at maximal spreading (2

1217   min). Shown is a representative kymograph of a CK-666-treated cell (**E**), relative lifetimes (**F**),

1218   and relative speeds (**G**) of inner F-actin foci in 30-sec windows before the inhibition and 10 sec

1219   after the inhibition in the same cells (linked by blue lines). (**H-J**) B-cells were treated with DMSO

1220   or Wisko (10 µM) 10 min before and during interaction with Fab'-PLB. Shown is a representative

1221   kymograph of a Wisko-treated B-cell **(H)**, relative lifetime **(I)**, and relative speed **(J)** of inner F-

1222   actin foci in DMSO versus Wisko-treated B-cells. (**K-M**) LifeAct-GFP-expressing WT and WKO

1223   B-cells were incubated with Fab'-PLB. Shown are a representative kymograph of a WKO B-cell

1224   **(K)**, relative lifetime (**L**), and relative speed (**M**) of WT versus WKO B-cells. Data points

1225   represent the averaged values from inner F-actin foci in individual cells, with 3 kymographs per

1226   cell and ~12 cells per condition per experiment from 3 independent experiments. Scale bar, 2

1227   μm. * p <0.05, ** p <0.01, *** p<0.001, by non-parametric and paired student's t-test.

1228

1229   **Figure 5. Inner F-actin foci, generated by N-WASP-activated Arp2/3, facilitate NMII**

1230   **recruitment and ring-like structure formation.** (**A-C**) B-cells from mice expressing the GFP

1231   fusion of non-muscle myosin IIA (GFP-NMIIA) transgene were treated with DMSO or Wisko (10

1232   μM) 10 min before and during incubation with Fab'-PLB. The B-cell contact zones were imaged

1233   live using TIRF. Shown are representative TIRF images of DMSO- and Wisko-treated B-cells at

1234   30 sec (during spreading) and 2 min 30 sec (after maximal spreading) post landing (**A,** Scale

1235   bars, 2 μm), the averaged GFP-NMIIA MFI (±SEM) (**B**), and the initial rates of increasing

1236   (±SEM) of GFP-NMIIA in the contact zone (the slope of the initial GFP-NMIIA MFI versus time

1237   curves of individual cells) (**C**). Data points represent individual cells from 3 independent

1238   experiments with ~6 cells per condition per experiment. * p <0.05, ***p<0.001, by Kolmogorov-

1239   Smirnov test (**B**) or non-parametric student's t-test (**C**). (**D**) Primary B-cells from mice

1240   expressing both GFP-NMIIA and LifeAct-RFP transgenes were incubated with Fab'-PLB at 37°C

1241   and imaged live by TIRF. Shown are a representative TIRF image of a cell and a kymograph

1242   generated from time-lapse TIRF images at the yellow line. The purple arrow indicates the

1243   starting point of contraction, the white arrow GFP-NMIIA recruitment proximal to the spreading

1244   membrane, and the yellow arrow an F-actin (LifeAct-RFP) focus originating at the lamellipodia

1245   and moving away from the spreading membrane. (**E, F**) Primary B-cells from flox control, WKO,

1246   and cNKO mice were incubated with Fab'-PLB for indicated times. Cells were fixed,

46

1247   permeabilized, stained for NMII light chain, and imaged by IRM and TIRF. Shown are

1248   representative IRM and TIRF images (**E**) and percentages (±SD) of B-cells with the NMII ring-

1249   like structure in individual images (**F**), identified by visual inspection. The data were generated

1250   from 3 independent experiments with 5 images per condition per experiment. Scale bars, 2 µm.

1251   * p <0.05, ** p <0.01, *** p<0.001, by non-parametric student's t-test.

1252   **Figure 5-Video 1.** Wiskostatin treatment inhibits NMII ring-like structure formation.

1253

1254   **Figure 6. B-cell contraction increases the molecular density within BCR clusters.** Primary

1255   B-cells from WT mice were treated with CK-689 or CK-666 from the beginning of the incubation

1256   with AF546-Fab'-PLB (0 min) or at the maximal B-cell spreading (2 min) (**A, D, E, H, I, N, O**).

1257   WT B-cells were treated with DMSO or Wisko (10 µM) 10 min before and during the incubation

1258   with AF546-Fab'-PLB (**B, F, J, P**). B-cells from flox control and cNKO mice were incubated with

1259   AF546-Fab'-PLB (**C, G, K, Q**). The B-cell contact zones were imaged live by TIRF. (**A-C**)

1260   Representative time-lapse images at 30 sec (during B-cell spreading) and 2 min 30 sec (after

1261   maximal spreading) after cell landed. Scale bars, 2 µm. (**D-G**) The MFI of AF546-Fab' in the

1262   contact zone was plotted over time. Purple rectangles indicate the contraction phase. (**H-K**)

1263   Rates of AF546-Fab' MFI increases in the B-cell contact zone before and during contraction

1264   were determined by the slope of AF546-Fab' MFI versus time plots. Data points represent

1265   individual cells and were generated from 3 independent experiments with 6-12 cells per

1266   experiment. * p <0.05, ** p <0.01, *** p<0.001, by Kolmogorov-Smirnov test (D-G) or paired

1267   student's t-test (H-K). (**L**) A representative frame from a time-lapse of a CK-689-treated B-cell

1268   (left) shows AF546-Fab' clusters 30 sec after contraction began, and enlarged time-lapse

1269   images (right) show a single AF546-Fab' cluster over a 40-sec time window after contraction

1270   began. AF546 clusters were identified using the criteria: $\geq$250 nm in diameter, $\geq$1.1 fold of FI

1271   outside the B-cell contact zone, and trackable for $\geq$ 20 sec. Scale bars, 2 µm. (**M**) The peak FI of

47

1272   an AF546-Fab' cluster was measured over time, and the increasing rate of AF546-Fab' peak FI

1273   of this cluster was determined by the slope of the plot. (**N-Q**) The rates (±SEM) of increase in

1274   AF546-Fab' peak FI in individual clusters were compared between during and after contraction

1275   (**N**), between B-cells treated with CK-689 and CK-666 from 0 min (**O**), between DMSO- and

1276   Wisko-treated B-cells (**P**), and between flox control and cNKO B-cells (**Q**) after B-cells reached

1277   maximal spreading. Data points represent individual cells, the averaged slopes of clusters

1278   detected in one B-cell, from 3 independent experiments with 6~12 cells per condition per

1279   experiment. *p <0.05, ** p <0.01, ***p<0.001, by non-parametric student's *t*-test.

1280   **Figure supplement 1.** Fab'-PLB, but not Tf-PLB, induces BCR clustering and phosphorylation.

1281   **Figure supplement 2.** Tracking and analyzing AF546-Fab' clusters in the B-cell contact zone.

1282   **Figure 6-Video 1.** Inhibition of B-cell contraction reduces the molecular density within BCR

1283   clusters.

1284

1285   **Figure 7. Increased molecular density in BCR clusters leads to reductions in BCR**

1286   **phosphorylation.** (**A-G**) Flox control and cNKO B-cells incubated with AF546-Fab'-PLB were

1287   fixed at 1, 3, 5, and 7 min, permeabilized, stained for phosphorylated CD79a (pCD79a,

1288   Tyr182), and imaged using TIRF and IRM. (**A**) Representative IRM and TIRF images of a flox

1289   control versus a cNKO B-cell at 7 min. Scale bars, 2 µm. (**B-D**) Ratios of pCD79a MFI relative to

1290   AF546-Fab' MFI were plotted against AF546-Fab' peak FI in individual AF546-Fab' clusters in

1291   the contact zone of flox control (**B**), cNKO B-cells (**C**), or flox control and cNKO B-cells overlay

1292   (**D**). AF546-Fab' clusters were identified as described in Figure 6 and Figure 6-figure

1293   supplement 2, from an equal number of cells at the 4 time points. Data points represent

1294   individual AF546-Fab' clusters with an equal number of clusters from each time point. The black

1295   diamond symbols represent the average ratios of pCD79a MFI to Fab' MFI in individual BCR-

1296   Fab' clusters within the indicated Fab' peak FI range. The brown square symbols represent the

1297   fraction of the AF546-Fab' clusters out of the total, within the indicated Fab' peak FI range. Data

1298   were generated from 3 independent experiments with ~20 cells and ≥125 clusters per condition

1299   per experiment. * *p* <0.05, *** *p*<0.001, by non-parametric student's *t*-test. (**E-G**) The MFI

1300   (±SEM) of AF546-Fab' (**E**) and pCD79a (**F**) and the MFI ratio (±SEM) of pCD79a relative to

1301   AF546-Fab' (**G**) in individual AF546-Fab' clusters at indicated times were compared between

1302   flox control and cNKO B-cells and between different times. (**H-K**) WT B-cells treated with CK-

1303   689 or CK-666 after 2 min-incubation with AF546-Fab'-PLB. (**H**) Representative IRM and TIRF

1304   images of a CK-689- versus a CK-666-treated B-cell at 7 min. Scale bars, 2 μm. (**I-K**) The MFI

1305   (±SEM) of AF546-Fab' (**I**) and pCD79a (**J**) and the MFI ratio (±SEM) of pCD79a relative to

1306   AF546-Fab' (**K**) in individual AF546-Fab' clusters were compared between CK-689- and CK-

1307   666-treated B-cells after 7 min stimulation. Data points represent individual clusters. Horizontal

1308   solid lines in the violin plots represent the mean, while the dotted lines represent the quartiles of

1309   the distribution. Data were generated from 3 independent experiments with ~20 cells per

1310   condition per experiment. * *p* <0.05, *** *p*<0.001, by non-parametric student's *t*-test. The *p*-

1311   values in **D** were corrected using the Benjamini-Hochberg/Yekutieli method for false discovery

1312   rate control.

1313

1314   **Figure 8. Effects of BCR-Fab' density on the association of Syk with BCR-Fab' clusters**

1315   **and its phosphorylation.** Primary B-cells from flox control and cNKO mice were incubated with

1316   AF546-Fab'-PLB at 37°C, fixed at 3 or 7 min, stained for total Syk and phosphorylated Syk

1317   (pSyk Y519/520), and imaged by TIRF. (**A-C**) Ratios of Syk MFI relative to AF546-Fab' MFI

1318   were plotted against AF546-Fab' peak IF in individual AF546-Fab' clusters in the contact zone

1319   of Flox control (**A**) and cNKO B-cells (**B**) and their overlay (**C**). AF546-Fab' clusters were

1320   identified as described in Figure 6 and Figure 6-figure supplement 2 from an equal number of

1321   cells after 3- and 7-min stimulation. Data points represent individual AF546-Fab' clusters with an

1322   equal number of clusters from each time point. The black diamond symbols represent the

1323   average ratios of Syk MFI to Fab' MFI in individual AF546-Fab' clusters with indicated Fab' peak

49

1324   FI ranges. The brown square symbols represent the fraction of the AF546-Fab' clusters out of

1325   the total at indicated Fab' peak PI ranges. (**D-F**) Ratios of pSyk MFI relative to AF546-Fab' MFI

1326   were plotted against AF546-Fab' peak IF in individual AF546-Fab' clusters in the contact zone

1327   of flox control (**D**) and cNKO B-cells (**E**) and their overlay (**F**). (**G-I**) MFI ratios of pSyk relative to

1328   AF546-Fab' were plotted against AF546-Fab' peak IF in individual pSyk puncta in the contact

1329   zone of Flox control (**G**) and cNKO B-cells (**H**) and their overlay (**I**). pSyk puncta were identified

1330   using the criteria: FI $\geq$1.3 fold of the background outside the B-cell contact zone and diameter

1331 $\geq$250 nm. The black diamond symbols represent the average ratios of pSyk MFI to Fab' MFI in

1332   individual AF546-Fab' clusters (**D-F**) or individual pSyk puncta (**G-I**) at indicated Fab' peak FI

1333   ranges. The brown square symbols represent the fraction of the AF546-Fab' clusters out of the

1334   total at indicated Fab' peak PI ranges. Data points represent individual AF546-Fab' clusters (**D-**

1335   **F**) or pSyk puncta (**G and H**), collected from an equal number of cells at 3 and 7 min. Data were

1336   generated from 3 independent experiments with ~23 cells per condition per experiment. * *p*

1337   <0.05, ** *p* <0.01, *** *p*<0.001, by non-parametric student's *t*-test, between AF546-Fab' cluster

1338   group with different Fab' peak FI ranges. The p-values in **C, F** and **I** were corrected using the

1339   Benjamini-Hochberg/Yekutieli method for false discovery rate control.

1340

1341   **Figure 9. The effects of BCR-Fab' density on the association of SHIP-1 with BCR-Fab'**

1342   **clusters and its phosphorylation.** Primary B-cells from flox control and cNKO mice were

1343   incubated with AF546-Fab'-PLB at 37°C, fixed at 3 or 7 min, stained for total SHIP-1 and

1344   phosphorylated SHIP-1 (pSHIP-1 Tyr1020), and imaged by TIRF. (**A-C**) Ratios of SHIP-1 MFI

1345   relative to AF546-Fab' MFI were plotted against AF546-Fab' peak IF in individual AF546-Fab'

1346   clusters in the contact zone of Flox control (**A**) and cNKO B-cells (**B**). An overlay of flox control

1347   and cNKO plots is also shown (**C**). AF546-Fab' clusters were identified as described in Figure 6

1348   and Figure 6-figure supplement 2 from an equal number of cells after 3 and 7 min stimulation.

1349   Data points represent individual AF546-Fab' clusters with an equal number of clusters from

1350   each time point. The black diamond symbols represent the average ratios of SHIP-1 MFI to Fab'

1351   MFI in individual AF546-Fab' clusters within indicated Fab' peak FI ranges. The brown square

1352   symbols represent the fraction of the AF546-Fab' clusters out of the total at indicated Fab' peak

1353   FI ranges. (**D-F**) Ratios of pSHIP-1 MFI relative to AF546-Fab' MFI were plotted against AF546-

1354   Fab' peak IF in individual AF546-Fab' clusters in the contact zone of flox control (**D**) and cNKO

1355   B-cells (**E**) and their overlay (**F**). (**G-I**) MFI ratios of pSHIP-1 relative to AF546-Fab' were plotted

1356   against AF546-Fab' peak IF in individual pSHIP-1 puncta in the contact zone of Flox control (**G**)

1357   and cNKO B-cells (**H**) and their overlay (**I**). The black diamond symbols represent the average

1358   ratios of pSHIP-1 MFI to Fab' MFI in individual AF546-Fab' clusters (**D-F**) or individual pSHIP-1

1359   puncta (**G-I**) at indicated Fab' peak FI ranges. The brown square symbols represent the fraction

1360   of the total clusters at indicated Fab' peak FI ranges. pSHIP-1 puncta were identified using the

1361   criteria: FI ≥1.5 fold of the background outside the B-cell contact zone and diameter ≥250 nm.

1362   Data points represent individual AF546-Fab' clusters (**D-F**) and pSHIP-1 puncta (**G and H**),

1363   collected from an equal number of cells at 3- and 7-min. Data were generated from 3

1364   independent experiments with ~23 cells per condition per experiment. * p <0.05, ** p <0.01, ***

1365 p<0.001, by non-parametric student's t-test, between AF546-Fab' cluster group with different

1366   Fab' peak FI ranges. The p-values in **C, F,** and **I** were corrected using the Benjamini-

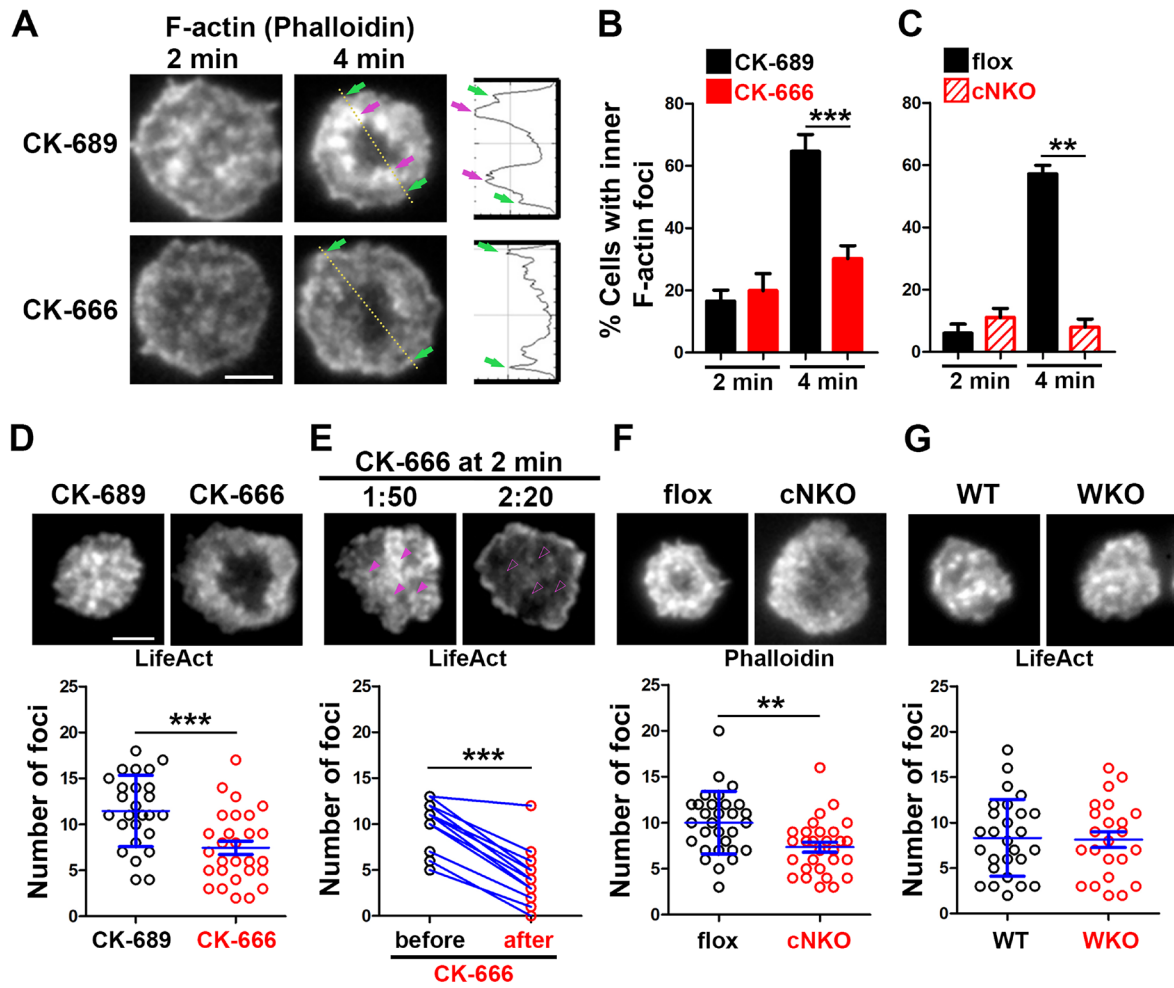1367   Hochberg/Yekutieli method for false discovery rate control.
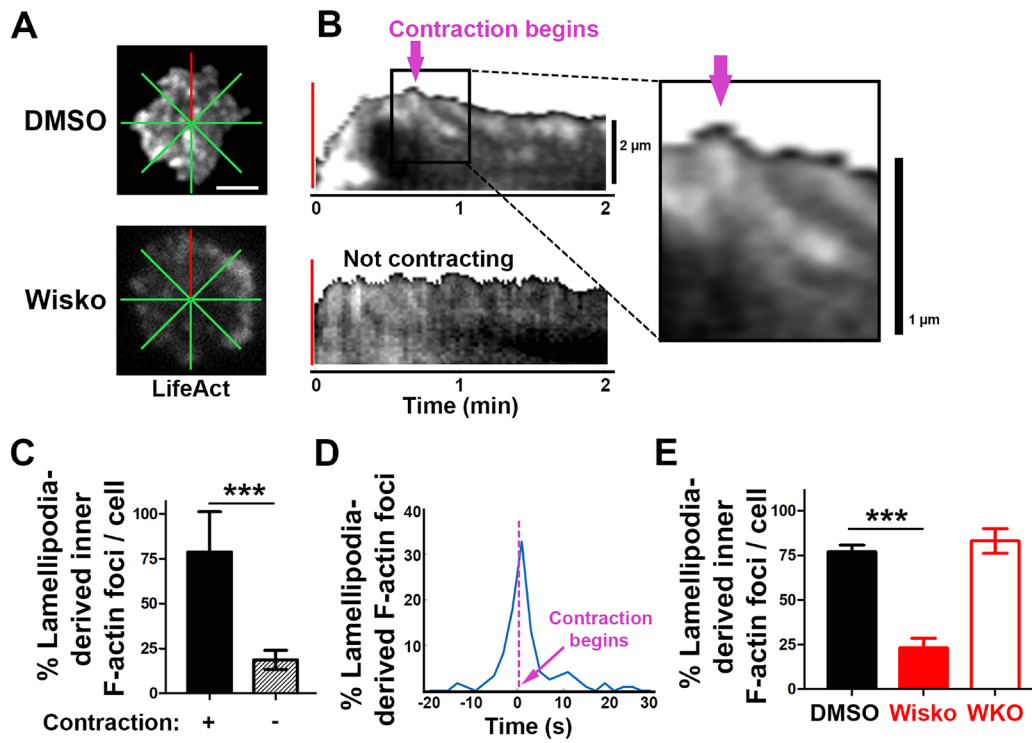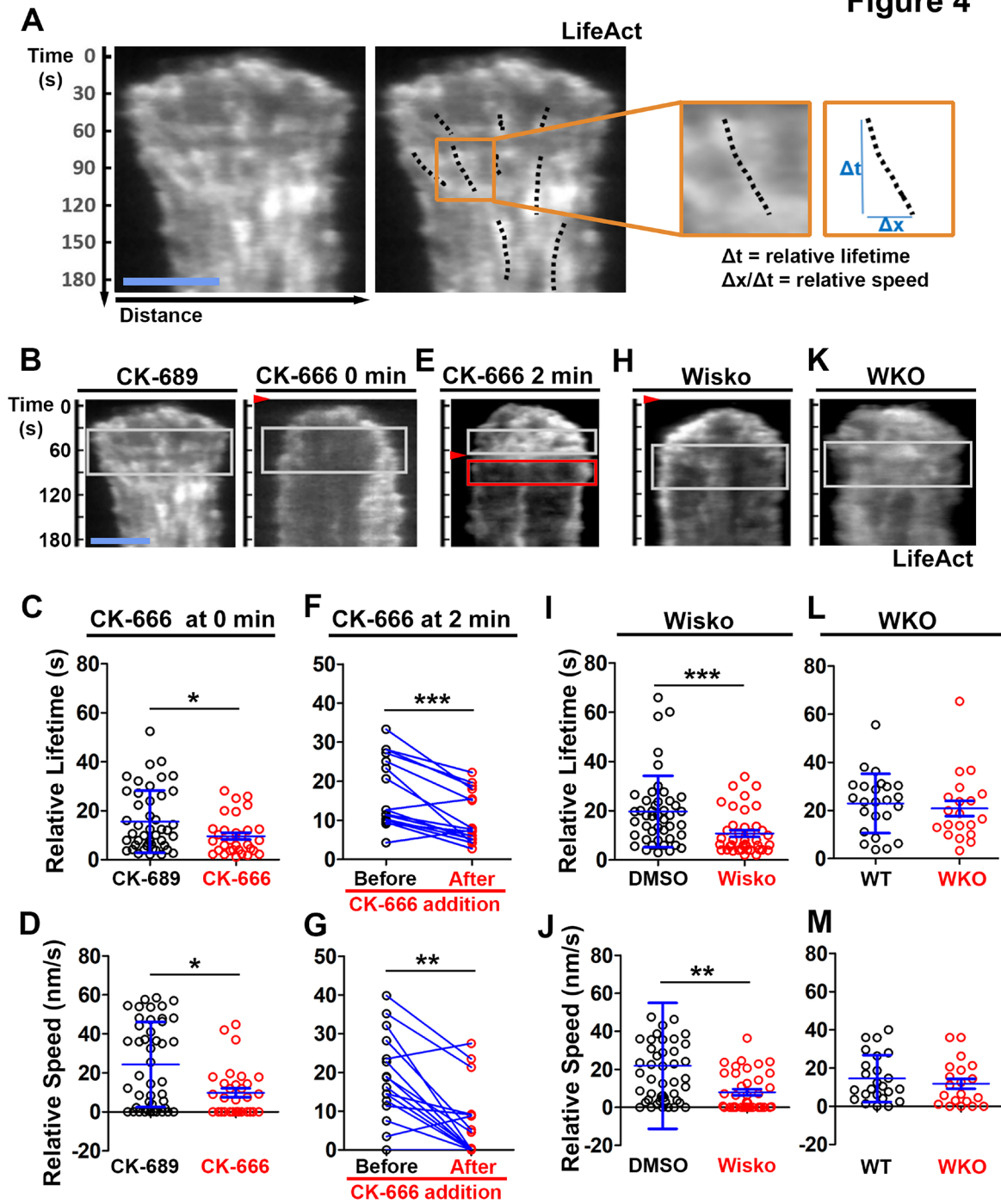
1368

Figure 1
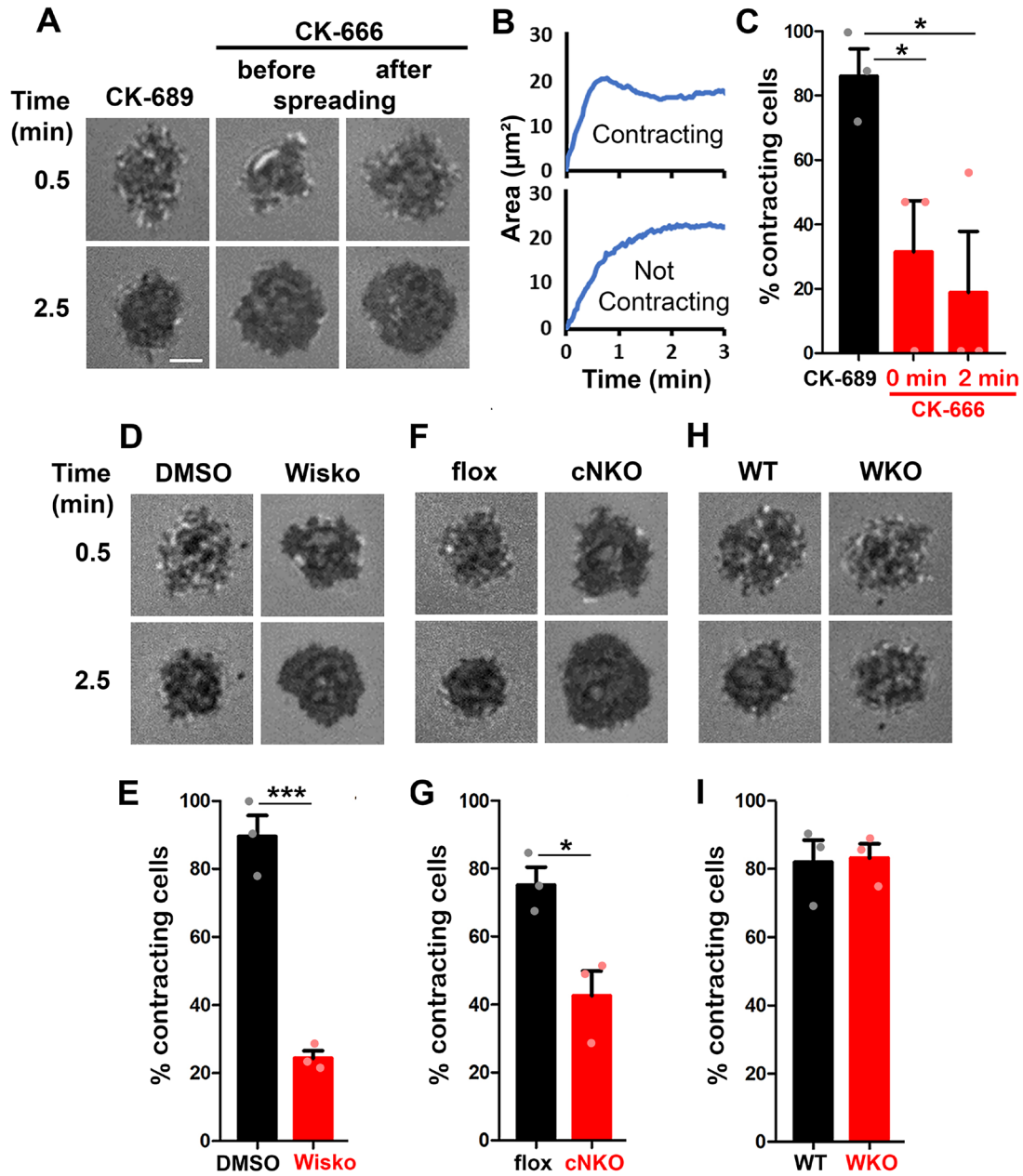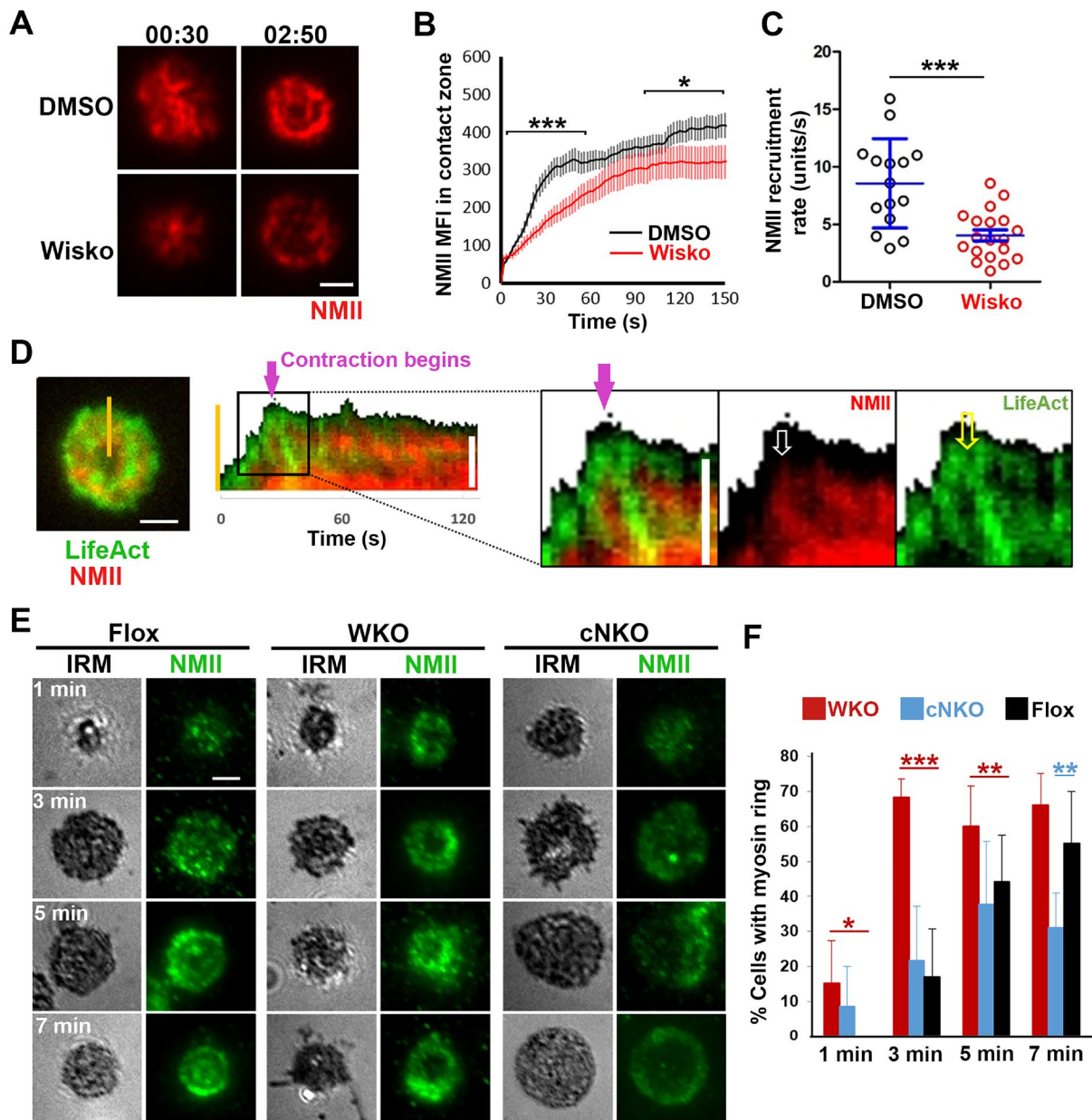

1369

1370

Figure 2

1371

1372

53

Figure 3

1373

1374

Figure 4

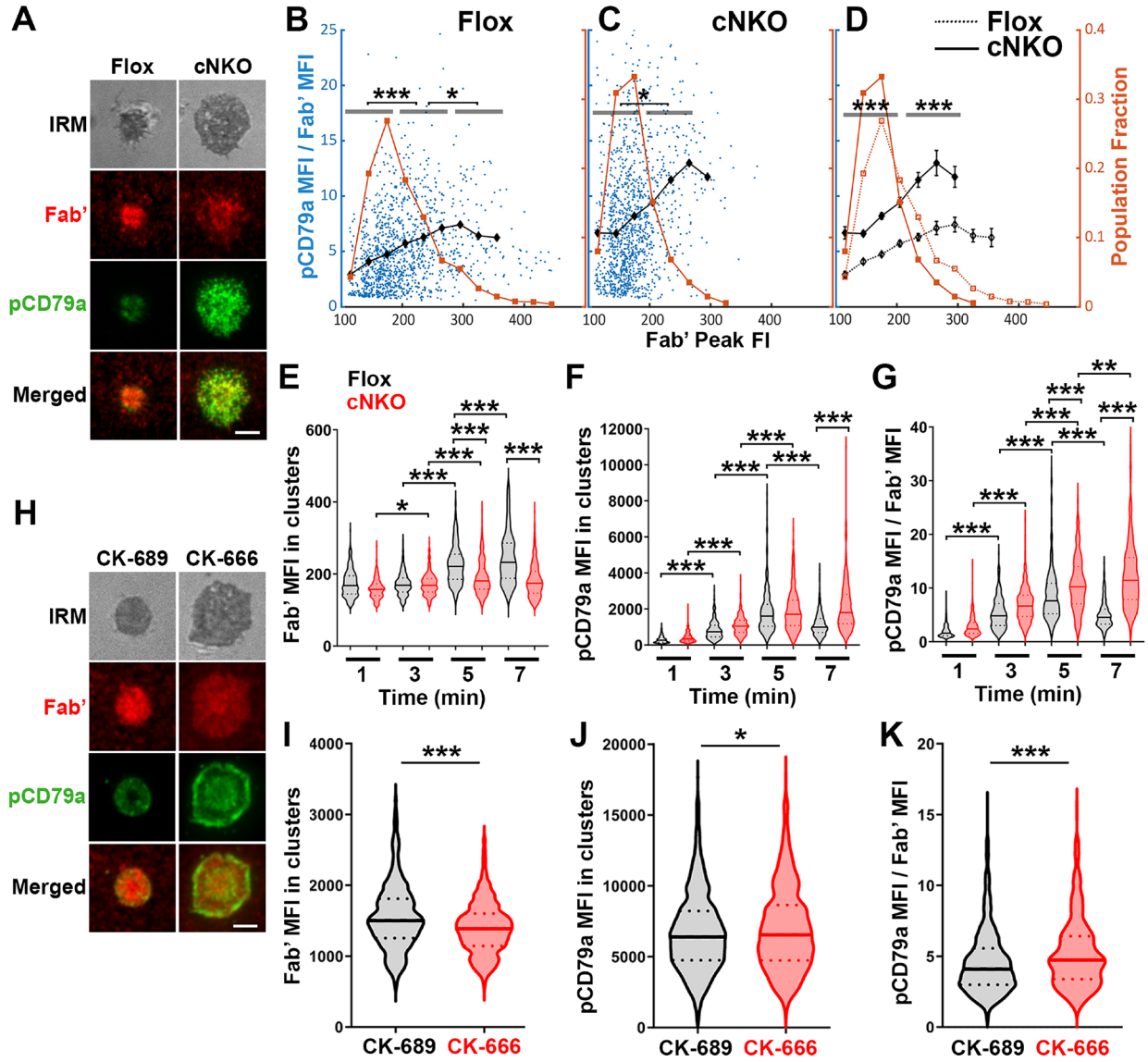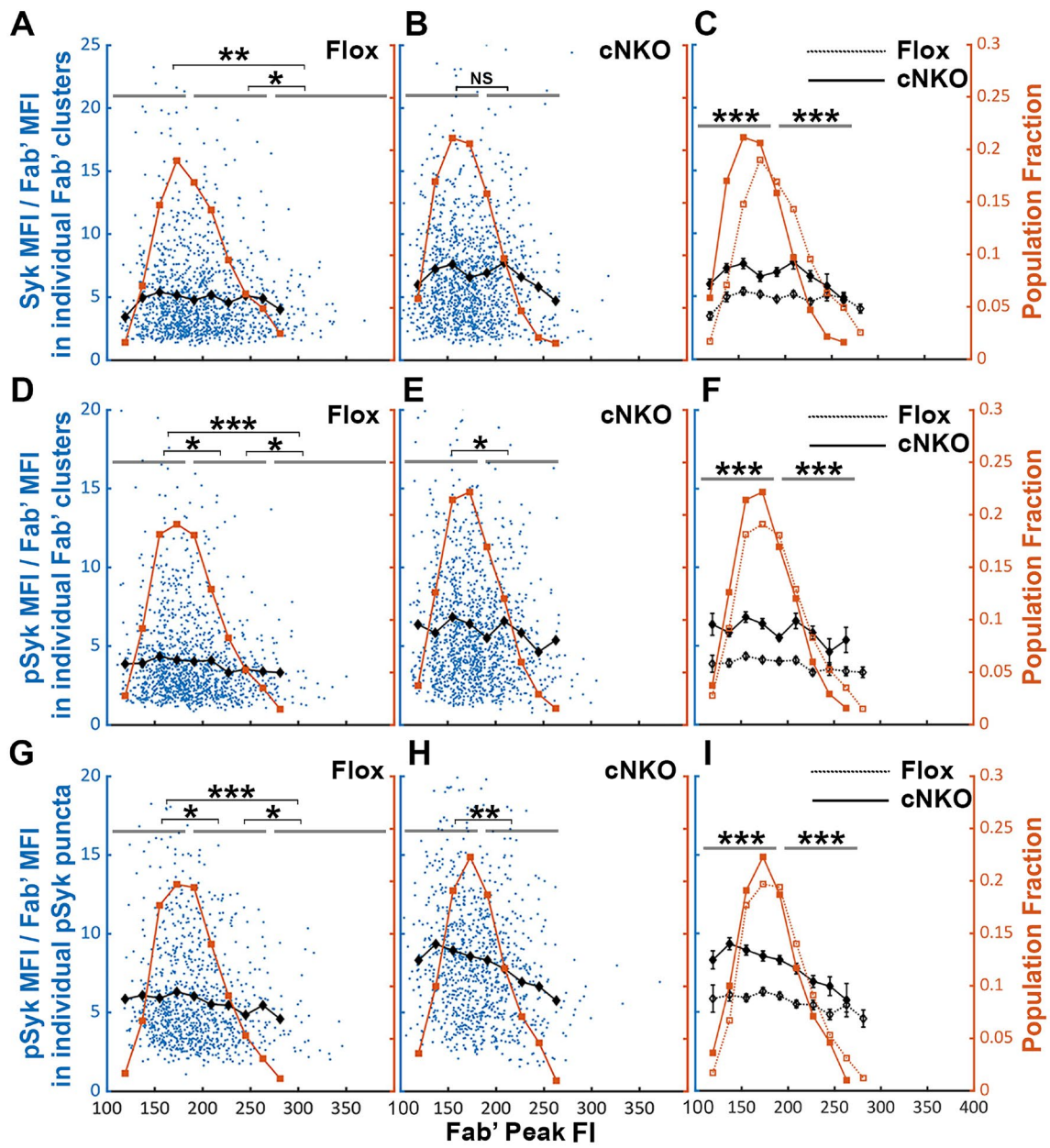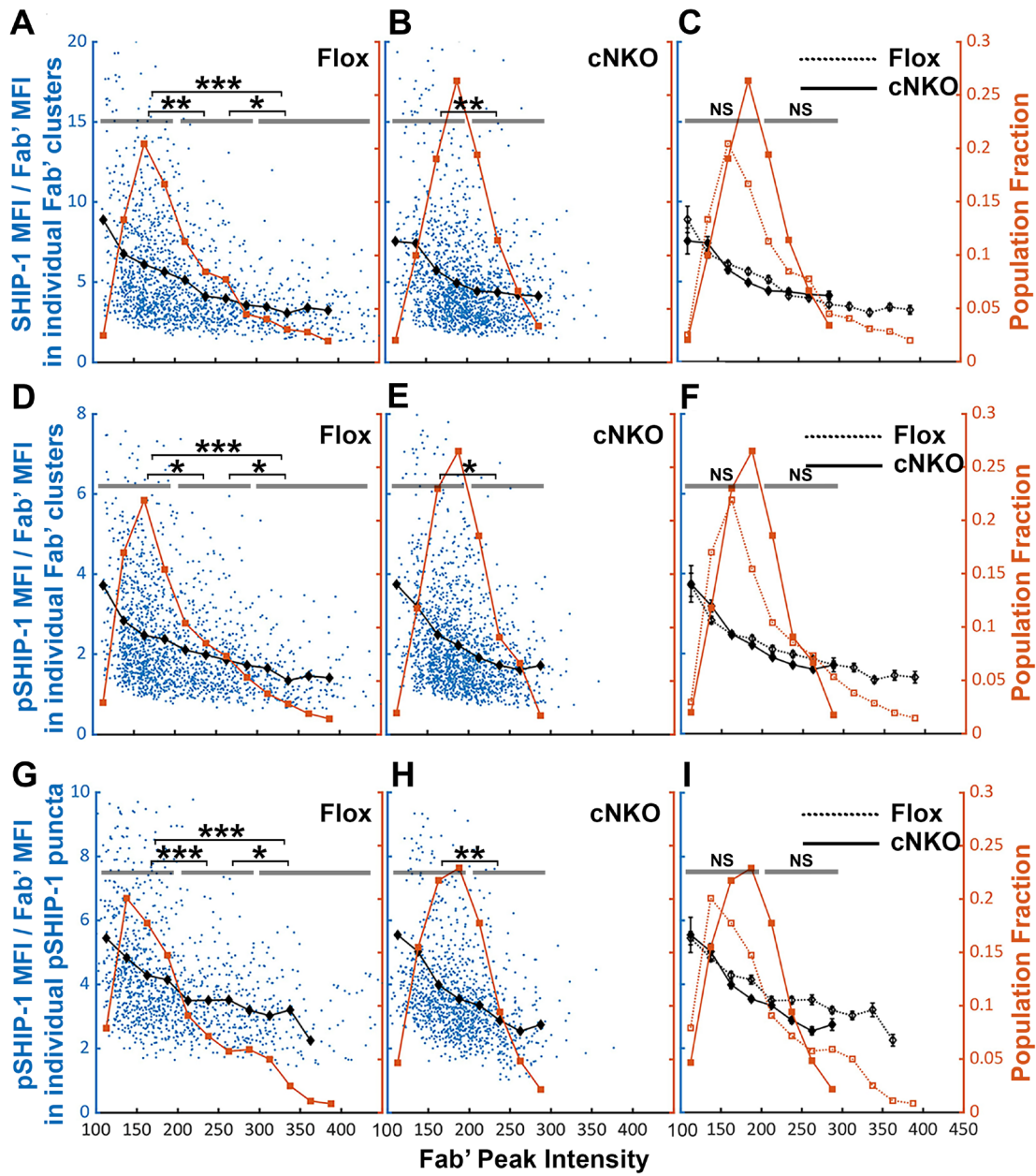**Figure 5**

1377

1378

Figure 6
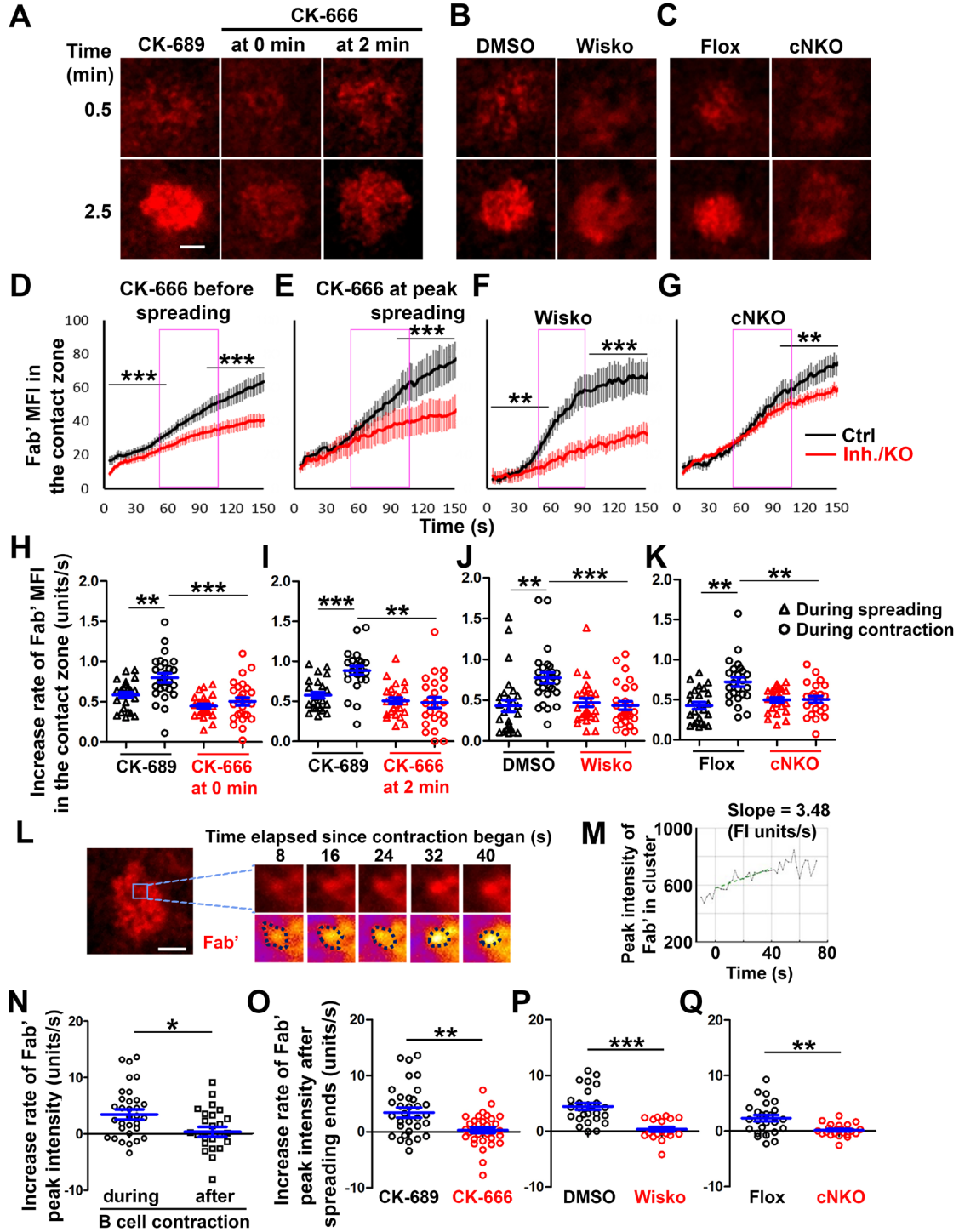
1379

1380

Figure 7

1381

1382

Figure 8

1383

1384

Figure 9

1385